

# Scaling relations of convective granulation noise across the HR diagram from 3D stellar atmosphere models

Luisa Fernanda Rodríguez Díaz,<sup>1\*</sup> Lionel Bigot<sup>2</sup>, Víctor Aguirre Børsen-Koch<sup>1</sup>, Mikkel N. Lund<sup>1</sup>, Jakob Lysgaard Rørsted<sup>1</sup>, Thomas Kallinger<sup>3</sup>, Sophia Sulis<sup>4</sup>, David Mary<sup>2</sup>

<sup>1</sup>*Stellar Astrophysics Centre, Department of Physics and Astronomy, Aarhus University, Ny Munkegade 120, DK-8000 Aarhus C, Denmark*

<sup>2</sup>*Université Côte d'Azur, Observatoire de la Côte d'Azur, CNRS, Lagrange UMR 7293, CS 34229, 06304, Nice Cedex 4, France*

<sup>3</sup>*Institute for Astrophysics (IfA), University of Vienna, Türkenschanzstrasse 17, 1180 Vienna, Austria*

<sup>4</sup>*Université Aix Marseille, CNRS, CNES, LAM, Marseille, France*

Accepted XXX. Received YYY; in original form ZZZ

## ABSTRACT

High-precision photometric data from space missions have improved our understanding of stellar granulation. These observations have shown with precision the stochastic brightness fluctuations of stars across the HR diagram, allowing us to better understand how stellar surface convection reacts to a change in stellar parameters. These fluctuations need to be understood and quantified in order to improve the detection and characterization of exoplanets. In this work, we provide new scaling relations of two characteristic properties of the brightness fluctuations time series, the standard deviation ( $\sigma$ ) and the auto-correlation time ( $\tau_{\text{ACF}}$ ). This was done by using long time series of 3D stellar atmosphere models at different metallicities and across the HR diagram, generated with a 3D radiative hydrodynamical code: the STAGGER code. We compared our synthetic granulation properties with the values of a large sample of *Kepler* stars, and analyzed selected stars with accurate stellar parameters from the *Kepler* LEGACY sample. Our 3D models showed that  $\sigma \propto \nu_{\text{max}}^{-0.567 \pm 0.012}$  and  $\tau_{\text{ACF}} \propto \nu_{\text{max}}^{-0.997 \pm 0.018}$  for stars at solar metallicity. We showed that both  $\sigma$  and  $\tau_{\text{ACF}}$  decrease with metallicity, although the metallicity dependence is more significant on  $\sigma$ . Unlike previous studies, we found very good agreement between  $\sigma$  from *Kepler* targets and the 3D models at  $\log g \leq 3.5$ , and a good correlation between the stars and models with  $\log g \geq 3.5$ . For  $\tau_{\text{ACF}}$ , we found that the 3D models reproduced well the *Kepler* LEGACY star values. Overall, this study shows that 3D stellar atmosphere models reproduce the granulation properties of stars across the HR diagram.

**Key words:** Stellar granulation – convection – hydrodynamics – stars: atmospheres – Kepler

## 1 INTRODUCTION

Thanks to photometric space missions such as *CoRoT* (Baglin et al. 2006), *Kepler* (Borucki et al. 2010) and *K2* (Howell et al. 2014) our knowledge about exoplanets orbiting distant stars has vastly increased, while also contributing to improving our understanding of stellar atmospheres. Particularly, these missions have driven the efforts of the last couple of years to model stellar granulation and stellar activity (see e.g. Pereira et al. 2019; Barros et al. 2020), with the aim to detect and characterize small exoplanets with TESS (Ricker et al. 2015) and PLATO (Rauer et al. 2014).

Many attempts have been made to characterize the stellar signal, both from theoretical and observational perspectives. From the theoretical approach, granulation noise properties have been studied using 3D radiation-hydrodynamic simulations of stellar atmospheres. Granulation is a time-dependent phenomenon associated with heat transport by convection on horizontal scales, due to radiative cooling (Nordlund et al. 2009). As a result, the stellar surface is filled with bright, hot granules and dark, cooler intergranular lanes. This interplay of hot up- and cool down-flows is also responsible for

brightness and temperature fluctuations over time on stellar surfaces. This is defined as stellar noise.

Trampedach et al. (1998); Ludwig (2006) proposed a formalism to use 3D stellar atmosphere models to derive disk-integrated brightness fluctuations, as seen by an observer. This formalism was implemented in Mathur et al. (2011), where they used 3D models at solar metallicity from Trampedach et al. (2013), to evaluate the granulation-induced fluctuations on the stellar brightness. They compared the results from the models with approximately 1000 red giant stars observed by *Kepler*, which they analyzed with six different techniques to fit their power spectra. They derived relations of granulation properties, namely power and timescale, in terms of the frequency of maximum power of the p-mode spectrum  $\nu_{\text{max}}$ , and showed that the 3D models could recover the same behavior that observations showed, but did not reproduce them accurately. Tremblay et al. (2013) used 148 3D model atmospheres from the CIFIST grid (Ludwig et al. 2009) to study their granulation properties. They found that the relative intensity and characteristic timescale ( $\tau_{\text{ACF}}$ ) are correlated with the Mach number, and to some extent with the Péclet number and convective efficiency. Similarly, Samadi et al. (2013) analyzed the power spectra of solar-metallicity 3D models from the CIFIST grid and determined their root-mean-square (rms) brightness

\* E-mail: luisa.rodriquez@phys.au.dk (LFRD)

fluctuations and  $\tau_{\text{ACF}}$ . Their results showed some scatter, especially for main-sequence (MS) models, when compared with  $v_{\text{max}}$ , i.e. an absence of a simple power law dependence  $v_{\text{max}}^{\alpha}$ . However, they found that the scatter decreases if the granulation properties are related to both  $v_{\text{max}}$  and the Mach number, with some combination of the two parameters. They also analyzed a small sample of stars observed by *Kepler*, but the dependency on the Mach number could not be confirmed. Additionally, Ludwig & Steffen (2016) used 3D stellar atmosphere models from the CIFIST grid with metallicities equal to  $[\text{Fe}/\text{H}] = 0.0$  and  $-2.0$  to study the metallicity effect on the brightness fluctuations. Even though their  $\sigma$  also increases with decreasing  $v_{\text{max}}$ , their data are scattered for both metallicities, similarly as the data presented in Samadi et al. (2013). They also claimed that they could not simultaneously fit the data at both metallicities, and neither could reproduce the  $\sigma$  values from Kallinger et al. (2014, hereafter K14), at least using the 3D solar metallicity models.

From the observational perspective, Bastien et al. (2013) found a clear correlation between brightness variations and surface gravity in *Kepler* light curves. This was done by isolating the variations related to granulation, corresponding to timescales shorter than 8 hours but longer than 30 minutes, called 8-hour flicker ( $F_8$ ) (see Bastien et al. 2016, for a more detailed description of the method). This relation points out that  $F_8$  decreases with surface gravity. However, this technique can only be applied for stars with  $\log g \geq 2.5$  dex –since stars with lower  $\log g$  deviated from their relation –, and does not provide good granulation timescales for MS stars, since they have granulation timescales shorter than 30 minutes. Cranmer et al. (2014) used existing scaling relations to derive the star-integrated variability of a sample of *Kepler* stars, and included an empirical correction factor for the magnetic suppression of convection in F-type stars. Pande et al. (2018) proposed a similar *Flicker* method, but calculating instead the Fourier power spectrum to measure the granulation background to determine  $\log g$  (see also Ness et al. 2018). Similarly, Bugnet et al. (2018) developed a slightly different tool called *FliPer*, which utilizes the average variability of a star measured in the power density spectrum at different frequency ranges. Additionally, Sulis et al. (2020b) introduced a new indicator to track the granulation properties (the flicker index), which is defined as the power density spectrum (PSD) slope in the frequency regime dominated by this stellar signal. They found again strong correlation with the stellar parameters, such as  $\log g$ . Van Kooten et al. (2021) improved the granulation flicker amplitude  $F_8$  for a large sample of *Kepler* stars, by incorporating the metallicity in the convective Mach number determination and using scaling relations derived from 3D models.

K14 analyzed the power spectra of red giants and MS stars observed by *Kepler*, from which they extracted their granulation and global oscillation parameters. As a result, they found a tight relationship between the granulation parameters,  $v_{\text{max}}$  and  $\log g$ . They also note some disagreement with the predictions of Samadi et al. (2013). Additionally, Kallinger et al. (2016) proposed a new method to determine a proxy for the characteristic timescale of the combined granulation and p-mode oscillation signal, as a tool to provide stellar surface gravities with accuracies of about 4%.

The study and understanding of stellar granulation also aims to constrain the stellar noise present in light curves or radial velocity measurements (see for example Sulis et al. 2020a). This is because the granulation noise might impose problems to detect Earth-size or smaller exoplanets, and might affect the determination of exoplanet parameters such as the planetary radius or mass. Evidence of this was shown for example by Meunier & Lagrange (2020), who found that granulation and supergranulation contribute significantly to the uncertainties of the planetary mass of an Earth-mass planet, espe-

cially for high-mass stars, when using radial velocities. Additionally, Sulis et al. (2020b) generated realistic exo-Earth transits on solar HMI observations, and demonstrated that the flicker noise could produce significant errors of up to 10% on the planetary radius.

To improve the understanding of the relation between granulation and stellar parameters, we provide in this paper a better characterization of the stellar brightness fluctuations by using for the first time very long time series (i.e. more than 1000 convective turnover times), from 3D stellar atmosphere models distributed across the Hertzsprung-Russell (HR) diagram. Particularly, for the first time, we show that both the standard deviation and auto-correlation time scale in terms of a simple power law  $\sim v_{\text{max}}^{\alpha}$ , and explore their dependencies with different metallicities. We found very good agreement when compared to observational *Kepler* data from K14, and a selected sample of stars with accurate stellar parameters.

The paper is structured as follows. In Section 2.1 we described the STAGGER-code and how the 3D stellar atmosphere models are generated. The sample of 3D models is described in Section 2.2 and a brief description of the code used to determine the radii of the 3D models is given in Section 2.3. Section 3 is devoted to the determination of granulation properties using the 3D models, and the derivation of power-laws in terms of  $v_{\text{max}}$ . The discussion of the metallicity effect on the granulation properties is in Section 3.3, and a comparison of our solar metallicity models with Samadi et al. (2013) is in Section 3.4. In Section 4, we present the comparisons with observational data, specifically with K14 and selected stars from the LEGACY sample (Lund et al. 2017). Finally, we discuss our results in Section 5 and conclude in Section 6.

## 2 THE 3D HYDRO-SIMULATIONS AND THEIR STELLAR PARAMETERS

### 2.1 The STAGGER-code

In this work, we used a standard version of the radiative-magnetohydrodynamic (R-MHD) STAGGER code (Nordlund & Galsgaard 1995; Nordlund et al. 2009; Magic et al. 2013), which generates 3D hydrodynamical model atmospheres that allow us to study stellar granulation across the HR diagram. The code solves the equations for the conservation of mass, momentum, and energy, as well as the radiative transfer equation under the assumption of local thermodynamic equilibrium (LTE). This equation is solved along a set of inclined rays specified by the user, which provides the heating and cooling rates needed for the energy equation. To account for the wavelength dependence of the radiative transfer we used the opacity binning method (Nordlund 1982; Skartlien 2000; Ludwig & Steffen 2013; Collet et al. 2018) to generate bins with an averaged opacity strength over specific wavelength ranges. The line opacities are taken from Gustafsson et al. (2008), while a sample of continuum absorption and scattering coefficients are adopted from Hayek et al. (2010). Furthermore, a realistic treatment of microphysics is included in the code, which accounts for ionization and molecule formation. This is done by using an improved version of the Equation of State (EOS) by Mihalas et al. (1988) obtained by Trampedach et al. (2013) (see their Section 2.1), which contains the 17 most abundant elements found in the Sun, plus  $\text{H}_2$  and  $\text{H}_2^+$ .

Every 3D simulation created with the STAGGER-code is defined by three stellar parameters: the entropy at the bottom that defines the effective temperature ( $T_{\text{eff}}$ ), surface gravity in logarithmic scale ( $\log g$ ) and metallicity ( $[\text{Fe}/\text{H}]$ ).  $T_{\text{eff}}$  is determined by the entropy –defined by both energy per unit volume and density– at the bottom boundary of every model, while the metallicity is defined by

the abundance of chemical elements. The models cover the upper radiative atmosphere or photosphere, the superadiabatic region, and the quasi-adiabatic deeper convective layers, where we ensure a flat entropy profile at the bottom of the simulation domain. These layers are distributed in a specific 3D Cartesian geometry. This means that the models are centered around the photosphere, and thus, only the top layers of a star are modeled.

The simulation domain contains typically ten granular cells (Magic et al. 2013) (see Fig. 1 for some examples). The sizes are a few tens of surface pressure scale heights in all directions. Thus, the areas increase for models representing evolved stars or for the earlier type stars. Since the boxes are very small compared to the size of the stars, gravity is assumed to be constant in the entire box. The simulation domain is periodic horizontally, and with open boundaries vertically.

One of the quantities that can be retrieved from the 3D models is the 2D surface intensity  $I(x, y, t)$ , as function of the horizontal Cartesian coordinates  $x$  and  $y$ , and time  $t$  of the snapshot. These intensities are used to compute the radiative bolometric flux defined as (see, for example Ludwig 2006)

$$F(t) = 2\pi \sum_{i=1}^{N_{\text{bins}}} \sum_{m=1}^{N_{\mu}} \sum_{k=1}^{N_{\phi}} w_{mk} (\cos \theta)_m \left\langle I_{mk}^{(i)}(x, y, t) \right\rangle, \quad (1)$$

where  $\left\langle I_{mk}^{(i)}(x, y, t) \right\rangle$  is the horizontal averaged intensity that corresponds to a given wavelength bin ( $i$ ) over the total number of bins  $N_{\text{bin}}$ . The flux is the sum over various inclination cosines  $(\cos \theta)_m$  angles where  $N_{\mu}$  indicates the number of rays, and  $N_{\phi}$  the sum over the fraction of solid angle  $w_{km}$  of the hemisphere at inclination  $\theta_m$  and azimuthal angles over  $k$ .  $w_{km}$  is defined by the Radau quadrature, multiplied by the constant weight over the azimuthal angle. For the 3D simulations used in this study we used  $N_{\mu} = 2$  and  $N_{\phi} = 4$ , and we justified this selection in Appendix A2.

The 2D intensity  $I_{km}^{(i)}(x, y, t)$  of a given bin ( $i$ ) is obtained by solving the (LTE) radiative transfer equation with the opacity binning method. Briefly, this method groups sets of wavelengths into a few bins based on the corresponding monochromatic continuous, line opacity, and their spectral interval (see Nordlund 1982; Ludwig 1992; Skartlien 2000; Stein & Nordlund 2003; Collet et al. 2018), instead of solving the full monochromatic radiative transfer.

Fig. 1 shows the bolometric intensity at a given time and for  $\cos \theta = 1$  for models representing a red giant star with  $T_{\text{eff}} = 5000$  K and  $\log g = 2.50$ , followed by a sub-giant star with  $T_{\text{eff}} = 5500$  K and  $\log g = 3.50$ , and a solar model. Each figure shows the granulation pattern, meaning bright hot granules surrounded by dark cooler intergranular lanes, which is a consequence of stellar convective up- and down-flows. The dimensions shown in the figure illustrate the fact that the granules increase in size as a star evolves, which is why the horizontal dimensions of our simulation boxes increase as well.

The 3D models also include box-modes (Nordlund & Stein 2001), which are acoustic modes generated by both the stochastic excitation and the work done by the bottom boundary. These modes have, however, excessively large amplitudes compared to the ones observed in stars due to the shallow boxes and, consequently, they have very low inertia. Such large amplitude modes would affect the convective brightness simulations in an unrealistic way. We therefore decided to artificially damp them, so the time series are free of them, as explained in Appendix A. This is a good approximation, since in stars, granulation contributes about 2–4 times as much as the oscillations depending on the evolutionary stage of the star (K14; Kallinger et al. 2016).

Finally, we emphasize that the models belong to an improved

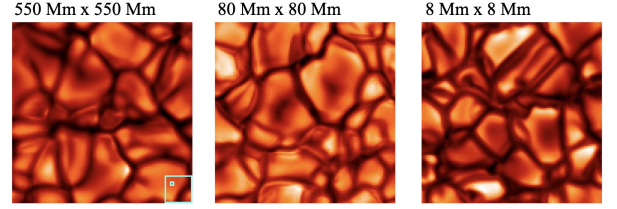


**Figure 1.** Disk centered surface intensities at specific times of stellar atmosphere models at solar metallicity. *Left:* a red giant  $T_{\text{eff}} = 5000$  K,  $\log g = 2.50$ . *Middle:* a sub-giant  $T_{\text{eff}} = 5500$  K,  $\log g = 3.50$ . *Right:* a solar-like star  $T_{\text{eff}} = 5777$  K,  $\log g = 4.44$ . The cyan scaled squares in the *left* panel are representations of the surface intensities in the *middle* and *right* panels.

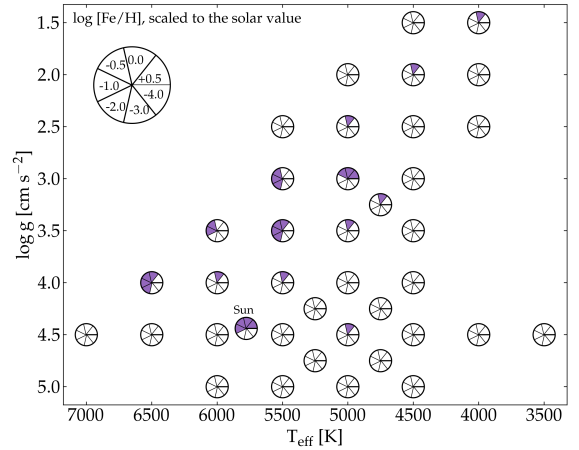


**Figure 2.** Kiel-diagram ( $T_{\text{eff}}$ - $\log g$ ) showing an updated version of the STAGGER-grid. Every pie chart represents models with a given  $T_{\text{eff}}$  and  $\log g$ , and metallicity decreases counterclockwise as illustrated in the figure. The models highlighted in purple correspond to the models included in our sample, while models in white are the rest of the models in our grid.

version of the STAGGER-grid (Rodríguez Díaz, in prep.), which was originally published in Magic et al. (2013) with more than 200 models distributed across the HR diagram, with metallicities between +0.5 and -4.0.

## 2.2 Sample of 3D stellar atmosphere models

Our sample of 3D stellar atmosphere models includes K-dwarfs to giant stars with metallicities  $[\text{Fe}/\text{H}] = +0.5, 0.0, -0.5, -1.0, -2.0$ , where the abundances of  $\alpha$ -elements for models with  $[\text{Fe}/\text{H}] \leq -1.0$  include  $\alpha$ -enhancement of +0.4 dex. The models are distributed across the Kiel-diagram as illustrated in Fig. 2. In Table 1 we summarized the stellar and physical parameters of our models, identified by their simulation names, which follow the nomenclature:  $txxgyymzz$  or  $txxgyypzz$ , where  $txx$  indicates the first two digits of  $T_{\text{eff}}$ ,  $gyy$  indicates  $\log g$ , and  $mzz$  or  $pzz$  indicate  $[\text{Fe}/\text{H}] \leq 0.0$  and  $[\text{Fe}/\text{H}] > 0.0$ , respectively.

Since the properties of convection change with stellar parameters, i.e.  $\log g$  and  $T_{\text{eff}}$ , we used a characteristic quantity to select the models for this work, that is, according to their frequency  $\nu_{\text{max}}$ . This quantity is defined as the ratio between sound speed to the pressure scale height, as  $\nu_{\text{max}} = c/H_p$ , where  $c$  scales roughly as  $(T_{\text{eff}}/\mu)^{1/2}$

with  $\mu$  representing the mean molecular weight, and  $H_p$  roughly as  $T_{\text{eff}}/g$ . We emphasize here that this frequency is well-known in asteroseismology since it corresponds to the maximum of the power of acoustic modes. Even if our analysis does not contain modes, we keep this quantity as defined in asteroseismology since it follows nicely the evolution of the star  $\nu_{\text{max}} \sim g/\sqrt{T_{\text{eff}}}$  (Belkacem et al. 2011). Low values of  $\nu_{\text{max}}$  correspond to evolved or hotter stars, while large values correspond to cool dwarfs. For the Sun its value is around  $3090 \mu\text{Hz}$ . Since we have models at different metallicities, we modified  $\nu_{\text{max}}$  according to the following dependencies:

$$\mu^{-1} = X + \frac{Y}{4} + \frac{Z}{\langle A \rangle}, \quad (2)$$

where  $\mu$  is the mean molecular weight,  $\langle A \rangle$  corresponds to the mean atomic number, which is  $\approx 15.5$  for our models, and the mass fractions  $X$ ,  $Y$ , and  $Z$  were directly determined from the chemical abundances of the simulations, keeping in mind that the abundances of alpha-elements for  $[\text{Fe}/\text{H}] \leq -1.0$  already accounted for  $\alpha$ -enhancement following

$$[\text{M}/\text{H}] = [\text{Fe}/\text{H}] + \text{corr}([\alpha/\text{Fe}]), \quad (3)$$

where *corr* makes reference to a correction factor based on  $[\alpha/\text{Fe}]$  (Salaris et al. 1993). Thus, the characteristic frequency  $\nu_{\text{max}}$  scales as (Viani et al. 2017)

$$\nu_{\text{max}} \propto \left( \frac{g}{g_{\odot}} \right) \left( \frac{T_{\text{eff},\odot}}{T_{\text{eff}}} \right)^{1/2} \left( \frac{\mu}{\mu_{\odot}} \right)^{1/2}, \quad (4)$$

where  $g_{\odot}$ ,  $T_{\text{eff},\odot}$ , and  $\mu_{\odot}$  correspond to the solar values. We note that for our 3D models, we used the following reference values, based on the solar-like 3D model at solar metallicity:  $g_{\odot} = 27542.29 \text{ cm/s}^2$ ,  $T_{\text{eff},\odot} = 5759 \text{ K}$ , and  $\mu_{\odot} = 1.249$ . We consider models of stars with 3 orders of magnitude range in  $\nu_{\text{max}}$ , as indicated in Table 1. To calculate  $\nu_{\text{max}}$  for every model, we used  $\langle T_{\text{eff}} \rangle$ , which is the mean  $T_{\text{eff}}$  from the time series, rather than the target  $T_{\text{eff}}$  corresponding to the  $T_{\text{eff}}$  that we aimed to achieve for each model. Hereafter, unless specified, the  $T_{\text{eff}}$  refers to  $\langle T_{\text{eff}} \rangle$ .

All 3D models in this work were generated with the following input physics:

- The time series covered at least 1000 convective turnover times, to have a reliable standard deviation independent of the length of the time series, opposite to what happens for too short time series of stochastic processes.
- Opacity tables with 6 bins were used if available, otherwise 12 bins were used. We note that the influence of the number of bins is negligible as shown in Appendix A1.
- The radiative transfer equation was solved along the vertical direction and 7 additional inclined angles.
- We used a grid resolution of 120 points in every direction.
- The box-modes were damped.

Since we computed long time series, saved at relative high cadence, the relative low grid resolution was chosen to minimize both the CPU and storage resources, without affecting the derived granulation properties. This is justified in Appendix A, where we studied the effects of our selection on the brightness fluctuations.

### 2.3 The Bayesian STellar Algorithm (BASTA)

Since the only stellar parameters that define the 3D models -  $T_{\text{eff}}$ ,  $\log g$ , and  $[\text{Fe}/\text{H}]$  - are indeed atmospheric parameters, it is not possible to describe a whole star with them. Therefore, several stars

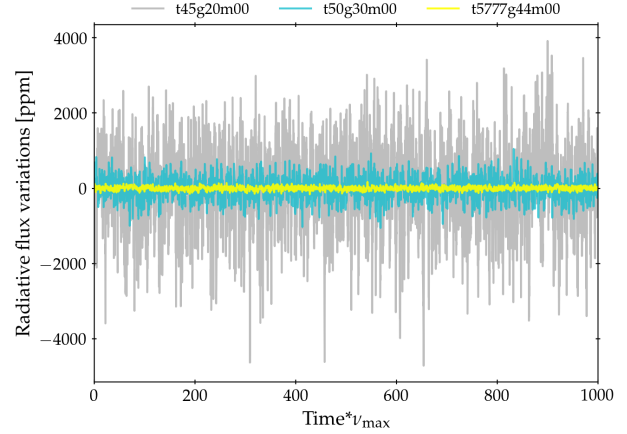


**Figure 3.** Comparison of the radiative flux variations as a function of the number of convective turnover times, for three simulated stars at different evolutionary stages: giant (t45g20m00) with  $\nu_{\text{max}} = 12.727 \mu\text{Hz}$ , subgiant (t50g30m00) with  $\nu_{\text{max}} = 121.516 \mu\text{Hz}$ , and a solar simulation (t5777g44m00) with  $\nu_{\text{max}} = 3106 \mu\text{Hz}$ .

with different radii, masses, and ages may match a given set of these parameters. As we will discuss in Sec. 3, to derive the  $\sigma$  of the brightness fluctuations of an *entire* star from a 3D model, we need to know its radius. In practice, to define the most *probable* star that matches any of our models, we use the Bayesian STellar Algorithm (BASTA; Silva Aguirre et al. 2015, 2017; Aguirre Børsen-Koch et al. 2021), a pipeline to accurately determine stellar properties using asteroseismology. A bayesian approach is implemented in BASTA to find the optimal solution from a pre-computed grid of evolutionary models, being in this study the grid of BaSTI isochrones (Hidalgo et al. 2018) that included overshooting, diffusion, and mass loss. This is done by taking prior information such as a standard Salpeter initial mass function, and providing a set of observables, being in this case  $T_{\text{eff}}$ ,  $\log g$ , and  $[\text{M}/\text{H}]$ .  $[\text{M}/\text{H}]$  was calculated using Eq. 3 with  $\alpha$ -enhancement  $[\alpha/\text{Fe}] = +0.4$  dex when appropriated, as this is not the case for all metallicities. BASTA then takes all this information into account to compute the probability of every model in the grid matching the observations. As a result, BASTA provides a posterior probability distribution (PDF) for every parameter, and the final values for each stellar quantity are taken as a robust estimate of a typical star configuration that matches the 16 and 84 percentiles of the distribution.

### 3 STELLAR CONVECTIVE NOISE FROM 3D STELLAR ATMOSPHERE MODELS

Granulation produces fluctuations of the bolometric radiative flux as a function of time. Fig. 3 shows models representing stars in the following stages: giant (t45g20m00), sub-giant (t50g30m00), and a solar simulation (t5777g44m00) in terms of the number of convective turnover times, defined here as the time from the time series scaled by the  $\nu_{\text{max}}$  associated with every model. From the figure it is clear, that the flux variations increase as a star evolves, and thus, increase with decreasing  $\nu_{\text{max}}$ .

This stochastic process can be described by two variables. First, its standard deviation  $\sigma$

$$\sigma_{\text{box}} = \sqrt{\langle \mathcal{F}^2 \rangle - \langle \mathcal{F} \rangle^2}, \quad (5)$$



**Table 1.** Stellar and physical parameters of the 3D stellar models used in this work. From left to right: model name, target effective temperature (target  $T_{\text{eff}}$ ) [K] corresponding to the  $T_{\text{eff}}$  that we aimed to achieve for each model, surface gravity in logarithm scale ( $\log g$ ) [ $\text{cm.s}^{-2}$ ], metallicity [Fe/H], mean  $\langle T_{\text{eff}} \rangle$  [K] from the time series, stellar radius [ $R_{\odot}$ ] calculated with BASTA using isochrones, area of each local box model [Mm x Mm], brightness fluctuations ( $\sigma$ ) [ppm], and effective timescale ( $\tau_{\text{ACF}}$ ) [s].

Model	Target $T_{\text{eff}}$ [K]	$\log g$ [ $\text{cm.s}^{-2}$ ]	$\langle T_{\text{eff}} \rangle$ [K]	[Fe/H]	Radius [ $R_{\odot}$ ]	$\nu_{\text{max}}$ [ $\mu\text{Hz}$ ]	$(lx)$ [Mm x Mm]	$\sigma$ [ppm]	$\tau_{\text{ACF}}$ [s]
t40g15m00	4000	1.50	3986	0.0	$27.640^{+0.821}_{-0.441}$	4.287	6600x6600	2139	150600
t45g20m00	4500	2.00	4522	0.0	$21.600^{+2.294}_{-5.137}$	12.727	2400x2400	1102	56730
t50g25m00	5000	2.50	4960	0.0	$15.671^{+0.612}_{-0.673}$	38.427	800x800	480	17160
t50g30p05	5000	3.00	4914	0.5	$8.926^{+0.862}_{-0.568}$	123.706	210x210	231	5328
t50g30m00	5000	3.00	4960	0.0	$6.048^{+0.356}_{-0.229}$	121.516	230x230	286	4852
t50g30m05	5000	3.00	4962	-0.5	$4.753^{+0.191}_{-0.133}$	120.914	200x200	289	4800
t55g30m05	5500	3.00	5508	-0.5	$7.734^{+0.467}_{-0.402}$	114.719	250x250	215	4835
t55g30m10	5500	3.00	5479	-1.0	$7.529^{+0.148}_{-0.162}$	115.043	250x250	205	4858
t55g30m20	5500	3.00	5545	-2.0	$6.733^{+0.037}_{-0.087}$	114.226	220x220	154	4170
t47g32m00	4750	3.25	4727	0.0	$3.613^{+0.045}_{-0.046}$	221.351	88.8x88.8	220	2490
t50g35m00	5000	3.50	4958	0.0	$2.886^{+0.076}_{-0.077}$	384.345	65x65	153	1559
t55g35m00	5500	3.50	5516	0.0	$3.834^{+0.151}_{-0.230}$	364.387	80x80	145	1591
t55g35m05	5500	3.50	5545	-0.5	$3.560^{+0.094}_{-0.093}$	361.888	64x64	118	1473
t55g35m10	5500	3.50	5430	-1.0	$3.251^{+0.086}_{-0.387}$	365.435	70x70	112	1489
t55g35m20	5500	3.50	5485	-2.0	$2.533^{+0.115}_{-0.033}$	363.186	60x60	97	1217
t60g35m05	6000	3.50	6004	-0.5	$3.614^{+0.017}_{-0.091}$	347.751	81x81	140	1585
t60g35m10	6000	3.50	5912	-1.0	$3.419^{+0.020}_{-0.072}$	350.221	80x80	127	1473
t60g40m00	6000	4.00	5962	0.0	$1.792^{+0.028}_{-0.028}$	1108.355	26x26	88	516
t65g40m00	6500	4.00	6413	0.0	$1.985^{+0.031}_{-0.035}$	1068.672	28x28	93	549
t65g40m05	6500	4.00	6485	-0.5	$1.761^{+0.029}_{-0.026}$	1058.205	27x27	84	462
t65g40m10	6500	4.00	6447	-1.0	$1.758^{+0.014}_{-0.027}$	1060.549	23x23	74	444
t65g40m20	6500	4.00	6440	-2.0	$1.651^{+0.000}_{-0.036}$	1059.841	20x20	72	422
t55g40m00	5500	4.00	5462	0.0	$1.646^{+0.028}_{-0.027}$	1157.975	23x23	85	474
t5777g44p05	5777	4.44	5775	0.5	$1.070^{+0.003}_{-0.002}$	3142.903	8x8	54	194
t5777g44m00	5777	4.44	5759	0.0	$0.994^{+0.009}_{-0.013}$	3106.000	8x8	46	195
t5777g44m05	5777	4.44	5767	-0.5	$0.900^{+0.010}_{-0.010}$	3090.649	8.3x8.3	40	188
t5777g44m10	5777	4.44	5743	-1.0	$0.787^{+0.056}_{-0.047}$	3094.855	7.5x7.5	36	190

which describes the deviation of the bolometric radiative flux around its mean value. Second, the auto-correlation time ( $\tau_{\text{ACF}}$ ) of the signal, which describes how long the fluctuations remain correlated in time. Our aim is to characterize these two quantities throughout the HR diagram, including their relation to fundamental stellar parameters and asteroseismic quantities. We note that the error bars associated to the power laws in this study correspond to standard errors of the fit, and thus, are 1-sigma error bars. This means that the errors only represent the deviation of our results with respect to the power laws.

### 3.1 Power law of standard deviation

We first extracted the average value of the bolometric radiative flux ( $\mathcal{F}$ ) at each time step (integrated over the 6 or 12 opacity bins), which can then be used to determine  $T_{\text{eff}}$  via the Stefan-Boltzmann law. The standard deviation ( $\sigma_{\text{box}}$ ) of the flux given by Eq. 1 is expressed in Eq. 5, which must be re-scaled by the number of granules  $N$  visible on the disk, corresponding to the ratio of areas of visible disk to box

surface, i.e.  $N = 2\pi R_{\star}^2 / l^2$ , where  $R_{\star}$  is the stellar radius, and  $l$  is the length of one horizontal side of the 3D models (see [Trampedach et al. 1998](#); [Ludwig 2006](#)):

$$\sigma = \sigma_{\text{box}} \sqrt{N^{-1}}. \quad (6)$$

This relation assumes that the stochastic process is ergodic and that all patches are statistically uncorrelated.

To determine  $\sigma$ , we first randomized the  $\mathcal{F}$  values of each time series by shuffling the order of the data points, to emulate the kind of signal a telescope will receive, that is a signal with contributions from the whole stellar disk. Subsequently, we calculated  $\sigma$  at cumulative intervals of five hours, to determine the value towards which  $\sigma$  converges.

Fig. 4 shows  $\sigma$  for some 3D stellar atmosphere models at solar metallicity, in terms of the number of convective turnover times. It can be seen that the brightness fluctuations increase as the star evolves towards the turn-off point and Red Giant Branch. For all targets, we found that at least 300 turnover convective times are needed to obtain

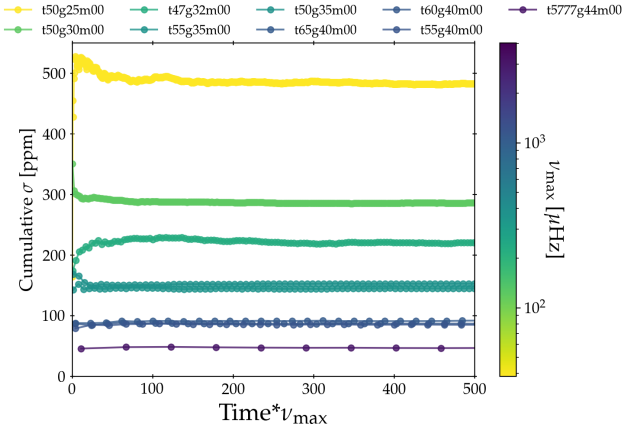


**Figure 4.** Cumulative standard deviation  $\sigma$  of the relative brightness fluctuations for the 3D stellar atmosphere models at solar metallicity, as a function of the number of convective turnover times. Each point in the plot represents the cumulative value of  $\sigma$  from 0 to the end of the time series, at intervals of five hours.

a reliable  $\sigma$  value. This means that RHD 3D simulations need to be long to perform reliable statistical studies of this noise source.

In order to analyze the relationship between the  $\sigma$  and stellar parameters, Fig. 5 shows the  $\sigma$  of our models at solar metallicity in terms of  $\nu_{\max}$ . The figure reproduces the fact that  $\sigma$  increases as  $\nu_{\max}$  decreases, as we have previously pointed out, and as some previous studies have shown (i.e. Mathur et al. 2011; Samadi et al. 2013, K14). However, our results show for the first time a very tight correlation expressed in terms of a single exponent of  $\nu_{\max}$ , i.e.  $\sim \nu_{\max}^{\alpha}$ , without the need to introduce an additional quantity (e.g. Mach number). We will expand more on this in Sec. 3.4. The power-law fit to our data indicates that

$$\sigma \propto \nu_{\max}^{-0.567 \pm 0.012}. \quad (7)$$

The slight deviations of individual models from the power-law are due to the determination of the radii, since their determination with BASTA is slightly less precise when using only the atmospheric parameters  $T_{\text{eff}}$ ,  $\log g$ , and  $[\text{Fe}/\text{H}]$  (see Fig. 8 in Aguirre Børsen-Koch et al. 2021).

### 3.2 Characteristic time scale $\tau_{\text{ACF}}$

We define the characteristic time of our time series as the auto-correlation time  $\tau_{\text{ACF}}$ , i.e. the time during which the fluctuations remain correlated in time. This is closely related to the convective turnover time. The auto-correlation function (ACF) of our time series is determined as the inverse Fourier transform of the PSD of the time series.  $\tau_{\text{ACF}}$  is defined to be the e-folding time of the ACF (see e.g. Mathur et al. 2011). In Fig. 5 we show the tight relation between  $\tau_{\text{ACF}}$  and  $\nu_{\max}$ , where it is clear that the more evolved the star is, the longer the timescale is. The power law shows that

$$\tau_{\text{ACF}} \propto \nu_{\max}^{-0.997 \pm 0.018}. \quad (8)$$

These 3D numerical results confirm the  $\sim 1/\nu_{\max}$  proposed by Kjeldsen & Bedding (2011), based on semi-empirical relation. It is indeed not surprising to find such dependence if we assume that the convective speed scales like the sound speed ( $c$ ) and the characteristic size scales like the pressure scale ( $H_p$ ), therefore the characteristic time must scale like  $\sim H_p/c \sim 1/\nu_{\max}$ .

### 3.3 Effects of metallicity

The granulation properties change with metallicity which have been found by numerical simulations (e.g. Nordlund & Dravins 1990; Magic et al. 2013; Ludwig & Steffen 2016) or from observations (e.g. for evolved stars Corsaro et al. 2017; Yu et al. 2018). Until now, the effects of metallicity on brightness fluctuations has never been investigated using 3D simulations with more than two different metallicities, which is what we explore in this section. We focus on how these brightness fluctuations change with the stellar parameters and metallicity.

In Fig. 6 we show the relation between  $\sigma$  and  $\tau_{\text{ACF}}$  with  $\nu_{\max}$  for every individual metallicity, i.e. 0.0, -0.5, -1.0, and -2.0. We excluded  $[\text{Fe}/\text{H}] = +0.5$  since our sample only contained two models at that metallicity. In Table 2 we summarized the power law relations between the granulation properties and  $\nu_{\max}$ . For the first time, 3D models are used to show that metallicity does have a significant impact on  $\sigma$ , as also found by Corsaro et al. (2017); Yu et al. (2018) using observations of evolved stars. We emphasize that they only considered evolved stars in their analysis and were restricted to a narrower range of metallicities. Specifically, we clearly show that  $\sigma$  decreases with metallicity, which is easily explained since the sizes of the granules also decrease with metallicity (Collet et al. 2007; Magic et al. 2013). Therefore,  $\alpha$  in  $\sigma \propto \nu_{\max}^{\alpha}$  decreases with metallicity. We want to mention that the model at highest  $\nu_{\max}$  at  $[\text{Fe}/\text{H}] = -2.0$  has a higher  $\sigma$  than expected, perhaps due to the horizontal dimensions of the model, which is why the trend looks different at that metallicity.

We fitted also a function of the form

$$\ln \left( \frac{\sigma}{\sigma_{\odot, 3D}} \right) = s \ln \left( \frac{\nu_{\max}}{\nu_{\max, 3D}} \right) + u[\text{Fe}/\text{H}], \quad (9)$$

similar to the fit used by Corsaro et al. (2017), where  $s$  and  $u$  are the constant to fit. We did not include the mass dependency as they did, since they used scaling relations to determine the mass for their targets, whereas the mass for the 3D models is determined with BASTA. We disregard the propagation of errors due to the determination of the stellar mass, therefore we do not include it in our results for simplicity. But using this equation to fit all the 3D models of our sample, we found that  $s = -0.556 \pm 0.010$ , and  $u = 0.211 \pm 0.033$ .

The relation derived by Corsaro et al. (2017) ( $u = 0.89 \pm 0.08$ ) was obtained for a restricted part of the power spectrum -at low frequencies- that they defined as meso-granulation. Despite the fact that we have very long simulated time series, they are still much shorter than the time series from *Kepler*. Therefore, in most of our simulations it was hard to see the different components of granulation in the power spectrum, or difficult to obtain a stable fit with Harvey laws. Instead, we extracted  $\sigma$  by computing the standard deviation in the time domain and not in the Fourier space. For this reason, we emphasize that our estimation of  $\sigma$  might slightly differ from those presented in Corsaro et al. (2017).

This explains why our  $u$  value is approximately 4 times lower than their value. We want to point out though, that they did not include the metallicity effect from the bolometric correction (see Lund 2019), which might have a small impact on their derived  $u$  parameter. In conclusion, we provide power-law relations between  $\sigma$  and  $\nu_{\max}$  for four different metallicities, and a general relation that has metallicity as one of its parameters, so that the reader can decide which one to use.

Additionally, we explore in the right panel of Fig. 6 the relation between  $\tau_{\text{ACF}}$  and  $\nu_{\max}$  for four different metallicities as well. Overall,

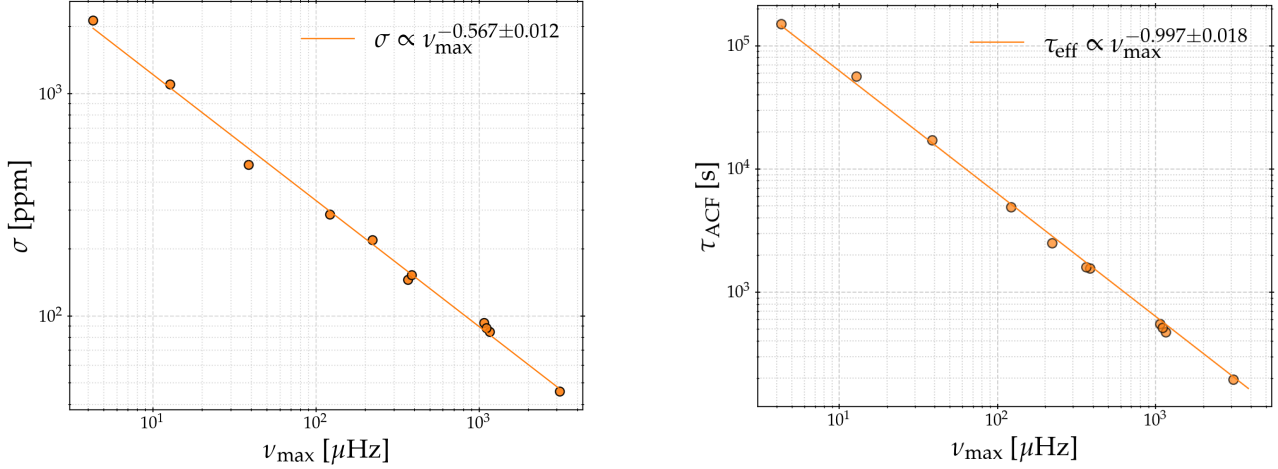


**Figure 5.** Standard deviation  $\sigma$  (left) and auto-correlation time  $\tau_{\text{ACF}}$  (right) for our sample of 3D models at solar metallicity, as functions of  $\nu_{\text{max}}$ .

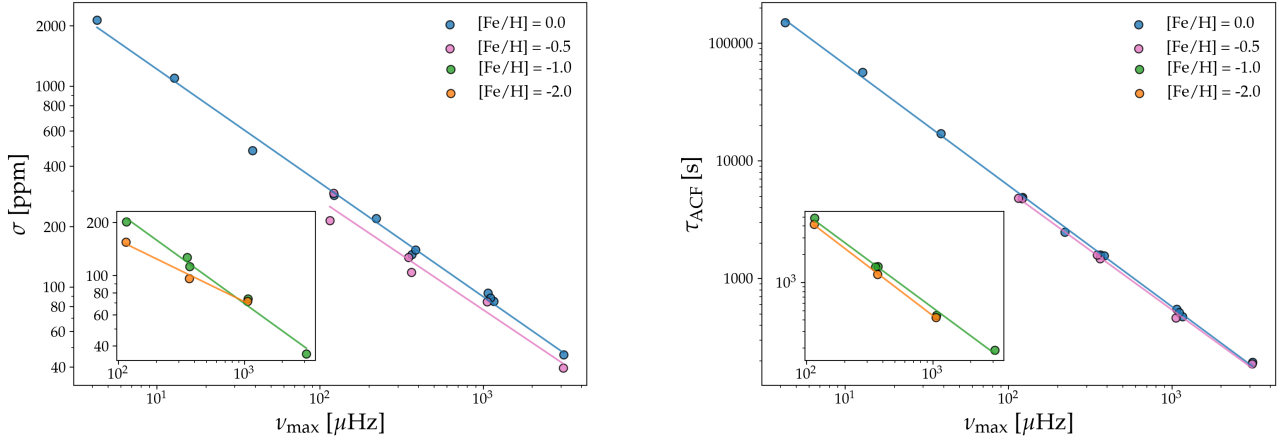


**Figure 6.** Standard deviations  $\sigma$  (left) and auto-correlation time  $\tau_{\text{ACF}}$  (right) as a function of metallicity. We clearly show a power law dependence between  $\sigma$  and  $\nu_{\text{max}}$  in terms of  $[\text{Fe}/\text{H}]$  (see text), where the coefficients decrease with metallicity.

**Table 2.** Values for the relation between  $\sigma$  and  $\tau_{\text{ACF}}$  with  $\nu_{\text{max}}$  for every  $[\text{Fe}/\text{H}]$ , as shown in Fig. 6.

$[\text{Fe}/\text{H}]$	$\sigma \propto \nu_{\text{max}}^{\alpha}$	$\tau_{\text{ACF}} \propto \nu_{\text{max}}^{\beta}$
0.0	$-0.567 \pm 0.012$	$-1.029 \pm 0.009$
-0.5	$-0.546 \pm 0.053$	$-1.009 \pm 0.025$
-1.0	$-0.516 \pm 0.034$	$-0.997 \pm 0.039$
-2.0	$-0.348 \pm 0.038$	$-1.029 \pm 0.022$

$\tau_{\text{ACF}}$  decreases slowly with metallicity, as also seen in the  $\beta$  values in Table 2 for the relation  $\tau_{\text{ACF}} \propto \nu_{\text{max}}^{\beta}$ , where it is clear that the timescales show a weak dependence on metallicity.

### 3.4 Comparison with Samadi et al. (2013)

Samadi et al. (2013) studied two granulation properties ( $\sigma$  and  $\tau_{\text{ACF}}$ ) of 3D models at solar metallicity using the CIFIST grid (Ludwig et al. 2009). They adopted a different method to analyze the models

**Table 3.**  $\alpha$  values from the relation between  $\sigma$  and  $\nu_{\text{max}}$  and between  $\tau_{\text{ACF}}$  and  $\nu_{\text{max}}$  from Fig. 7, for the 3D models of this study and the 3D models of Samadi et al. (2013)

Relation	$\alpha$ - This study	$\alpha$ - (Samadi et al. 2013)
$\sigma \propto \nu_{\text{max}}^{\alpha}$	$-0.567 \pm 0.012$	$-0.513 \pm 0.062$
$\tau_{\text{ACF}} \propto \nu_{\text{max}}^{\alpha}$	$-0.997 \pm 0.018$	$-0.944 \pm 0.019$

compared to the method used in this work, where they fitted the power spectrum of the times series using Harvey laws to extract their parameters.

Fig. 7 shows  $\sigma$  as a function of  $\nu_{\text{max}}$  for the 3D models for the two analyses. In each case, we determined the relation  $\sigma \propto \nu_{\text{max}}^{\alpha}$  for both samples, which are summarized in Table 3. Despite the fact that the power  $\alpha$  in the two studies are within the 1-sigma agreement (see Table 3), the  $\sigma$  values determined by Samadi et al. (2013) show a strong scatter that we do not observe in our sample, allowing us to associate a unique  $\sigma$  value for a given  $\nu_{\text{max}}$ , something that was not

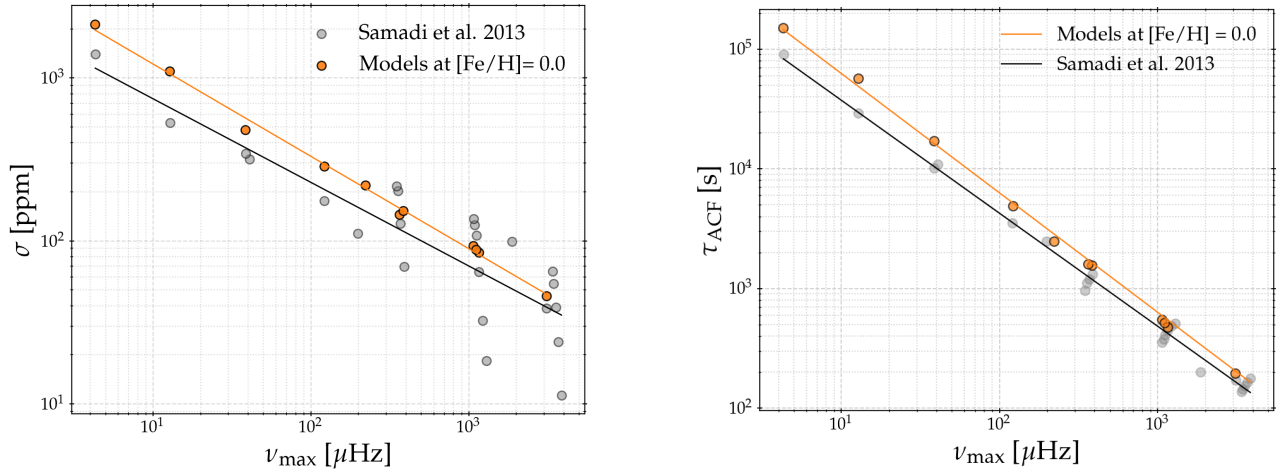


**Figure 7.** Comparison of standard deviations  $\sigma$  (Left) and auto-correlation times  $\tau_{\text{ACF}}$  (Right), as functions of  $\nu_{\max}$ , between our sample and the one presented by Samadi et al. (2013). The orange and black power law fits correspond to the fits of our data and Samadi et al. (2013) data, respectively, whose information is listed in Table 3.

possible in Samadi et al. (2013). In order to derive a power-law like behavior they introduced a different reference quantity  $\sim z_3^\alpha$  which accounts for the Mach number, in order to decrease the scatter of the  $\sigma$  values. Our results show that there is no need to introduce such dependence, and  $\sigma$  can be derived with only knowing the stellar parameters.

Given that both the STAGGER and CO<sup>5</sup>BOLD codes have similar physics and structures, we attribute the different behavior to two main reasons: their short time series and their radius determination. Since their time series were only about 9 hours long for solar-like stars (Ludwig H.-G. private comm.), this might introduce an incorrect  $\sigma$  by about 2-6%, based on the early fluctuations associated with  $\sigma$  in Fig. B1. Nevertheless, these fluctuations do not account for all the differences seen in Fig. 7. Regarding the stellar radii, they did not provide enough information about how the values were determined. Nevertheless, we know that those values depend on the atmospheric parameters of the 3D models, and the method and underlying physical assumptions used to calculate the radii. If the proper conditions are not chosen, the code might provide an incorrect stellar radius. By comparing the radii values from Samadi et al. (2013) and the ones determined in this work with BASTA for the models with similar or equal  $T_{\text{eff}}$ ,  $\log g$ , and  $[\text{Fe}/\text{H}]$ , we found that the values reported by Samadi et al. (2013) are overestimated, especially for models with  $\log g \leq 3.0$ . For example, for the t40g15m00 models, the radius difference is of  $12.18R_\odot$ , while for the t50g25m00 models the difference is  $2.579R_\odot$ . Another possible reason that might contribute to the observed scatter in Samadi et al. (2013) is, that the box modes were not damped (Ludwig, Private comm) in their study, opposite to our approach.

Regarding the timescales  $\tau_{\text{ACF}}$ , we show in Fig. 7  $\tau_{\text{ACF}}$  of our solar metallicity models with the values reported by Samadi et al. (2013), as a function of  $\nu_{\max}$ . The figure shows that we recover the same trend. In fact, our relation  $\tau_{\text{ACF}}(\nu_{\max})$  shown in Eq. 8 is in better agreement with the relation derived by Kjeldsen & Bedding (2011), i.e.  $\tau_{\text{ACF}} \propto \nu_{\max}^{-1}$ . Even though both power laws are very similar, it is worth mentioning that Samadi et al. (2013) data for  $\nu_{\max}$  higher than  $120 \mu\text{Hz}$  present a relatively significant scatter of up to  $\sim 500$  s, contrary to the data presented in this study. Therefore, we can again provide a unique value of  $\tau_{\text{ACF}}$  for a given set of stellar parameters.

#### 4 COMPARISON WITH KEPLER STARS

We aim to compare our theoretical predictive power laws with a sample of stars observed by the *Kepler* space mission, which observed more than 145,000 stars for more than four year. The observations were either carried out in long cadence (LC) of  $\sim 30$  min or short cadence (SC) of  $\sim 1$  min. We refer to Borucki et al. (2010) for more detailed information about the Kepler mission.

In this study, we used two different samples of *Kepler* stars, which will be introduced below. The first sample corresponds to the stars analyzed in K14 (see their Sec. 2), where they focused on LC data of 1289 red-giant stars that had previously been used in other studies (see references therein), and SC data of 75 sub-giant and solar-type stars, originally presented in Chaplin et al. (2011b). The stellar parameters of these stars were obtained from scaling relations. The second sample corresponds to the LEGACY stars (Lund et al. 2017), which are MS stars with frequency-power spectra optimized for asteroseismology. The selected stars together with their stellar parameters are shown in Table. 4. We emphasize that the stellar parameters obtained from the fit of the individual mode frequencies are more accurate than those obtained from simple scaling relations. For the LEGACY sample, we used the data in Lund et al. (2017). We point out, that three stars of the LEGACY sample are in common with the sample of K14, specifically KIC 6106415, KIC 5184732, and KIC 12317678.

##### 4.1 Determination of granulation properties of our selected stars (LEGACY)

To determine the  $\sigma$  values for the selected sample of LEGACY stars, we decided to fit the background model of the power spectra, instead of using the power-law relations derived in the previous section. This with the aim of verifying that different techniques can yield similar results, and thus, use observations to validate the power-laws derived using the 3D stellar atmosphere models.

The power spectrum was calculated from a weighted least-square sine-wave fitting to the time series (see Handberg & Lund 2014; Lund et al. 2017, for more details). We fit for each star a background



**Table 4.** Stellar properties and statistical uncertainties of selected stars from the LEGACY sample (Lund et al. 2017).  $\sigma$  values were determined by fitting their power spectrum. An example of this fitting is shown in Appendix E

KIC	$T_{\text{eff}}$ [K]	$\log g$ [cm.s <sup>-2</sup> ]	[Fe/H]	$\sigma$ [ppm]	$\tau_{\text{ACF}}$ [s]	$\nu_{\text{max}}$ [ $\mu$ Hz]
Sample of LEGACY stars						
3656476	5668 $\pm$ 77	4.225 <sup>+0.010</sup> <sub>-0.008</sub>	0.25 $\pm$ 0.10	59.162 <sup>+0.298</sup> <sub>-0.310</sub>	308.394 <sup>+4.662</sup> <sub>-4.803</sub>	1925
5184732	5846 $\pm$ 77	4.255 <sup>+0.008</sup> <sub>-0.010</sub>	0.36 $\pm$ 0.10	55.078 <sup>+0.149</sup> <sub>-0.143</sub>	297.757 <sup>+3.496</sup> <sub>-3.484</sub>	2089
6106415	6037 $\pm$ 77	4.295 <sup>+0.009</sup> <sub>-0.009</sub>	-0.04 $\pm$ 0.10	45.647 <sup>+0.145</sup> <sub>-0.138</sub>	262.891 <sup>+3.499</sup> <sub>-3.709</sub>	2249
6679371	6479 $\pm$ 77	3.934 <sup>+0.008</sup> <sub>-0.007</sub>	0.01 $\pm$ 0.10	67.988 <sup>+0.533</sup> <sub>-0.494</sub>	510.592 <sup>+16.871</sup> <sub>-19.017</sub>	942
7106245	6068 $\pm$ 102(3)	4.310 <sup>+0.008</sup> <sub>-0.010</sub>	-0.99 $\pm$ 0.19(3)	44.448 <sup>+1.487</sup> <sub>-1.578</sub>	254.292 <sup>+25.088</sup> <sub>-25.214</sub>	2398
7296438	5775 $\pm$ 77	4.201 <sup>+0.010</sup> <sub>-0.009</sub>	0.19 $\pm$ 0.10	58.894 <sup>+0.524</sup> <sub>-0.505</sub>	313.926 <sup>+9.521</sup> <sub>-8.071</sub>	1848
7871531	5501 $\pm$ 77	4.478 <sup>+0.005</sup> <sub>-0.007</sub>	-0.26 $\pm$ 0.10	32.139 <sup>+0.257</sup> <sub>-0.294</sub>	244.392 <sup>+6.820</sup> <sub>-5.699</sub>	3456
7970740	5309 $\pm$ 77	4.539 <sup>+0.005</sup> <sub>-0.004</sub>	-0.54 $\pm$ 0.10	30.866 <sup>+0.123</sup> <sub>-0.119</sub>	232.506 <sup>+2.666</sup> <sub>-2.423</sub>	4197
8006161	5488 $\pm$ 77	4.494 <sup>+0.007</sup> <sub>-0.007</sub>	0.34 $\pm$ 0.10	42.786 <sup>+0.862</sup> <sub>-0.378</sub>	186.484 <sup>+15.512</sup> <sub>-4.209</sub>	3575
9025370	5270 $\pm$ 180(2)	4.423 <sup>+0.004</sup> <sub>-0.007</sub>	-0.12 $\pm$ 0.18(2)	30.047 <sup>+0.266</sup> <sub>-0.282</sub>	227.339 <sup>+5.452</sup> <sub>-4.565</sub>	2989
9098294	5852 $\pm$ 77	4.308 <sup>+0.007</sup> <sub>-0.005</sub>	-0.18 $\pm$ 0.10	46.229 <sup>+0.451</sup> <sub>-0.473</sub>	253.942 <sup>+7.846</sup> <sub>-7.461</sub>	2315
12069127	6276 $\pm$ 77	3.912 <sup>+0.004</sup> <sub>-0.005</sub>	0.08 $\pm$ 0.10	63.718 <sup>+2.292</sup> <sub>-1.613</sub>	489.342 <sup>+49.358</sup> <sub>-67.995</sub>	885
12258514	5964 $\pm$ 77	4.126 <sup>+0.003</sup> <sub>-0.004</sub>	-0.00 $\pm$ 0.10	56.478 <sup>+0.153</sup> <sub>-0.154</sub>	374.428 <sup>+5.441</sup> <sub>-5.737</sub>	1513
12317678	6580 $\pm$ 77	4.048 <sup>+0.009</sup> <sub>-0.008</sub>	-0.28 $\pm$ 0.10	57.130 <sup>+0.461</sup> <sub>-0.401</sub>	353.875 <sup>+10.962</sup> <sub>-14.398</sub>	1212

model of the power spectrum of the form (Harvey 1985, K14)

$$P(\nu) = P_n + \eta^2(\nu) \left[ \sum_{i=1}^3 \frac{\xi_i \sigma_i^2 \tau_i}{1 + (2\pi\nu\tau_i)^{a_i}} + G(\nu) \right]. \quad (10)$$

Here  $\eta(\nu)$  describes the apodization of the signal amplitude (square root of power) at frequency  $\nu$  from the finite sampling, and in effect binning, of the temporal signal (Chaplin et al. 2011a);  $\tau_i$  gives the characteristic time scale of the  $i$ th background component;  $\sigma_i$  gives the corresponding  $\sigma$  variation of the component in the time domain;  $P_n$  denotes a constant shot-noise level;  $a_i$  gives the slope of the decay, and thus the amount of memory in the background phenomenon (a value of 2 corresponds to a standard Harvey model);  $\xi_i$  is a normalisation constant such that the integral of the background equals  $\sigma_i^2$  in accordance with Parseval's theorem (see, e.g., Michel et al. 2009). To determine the total  $\sigma$  to compare with the  $\sigma$  of our 3D models, we computed  $\sqrt{\sigma_1^2 + \sigma_2^2}$ , where  $\sigma_1$  and  $\sigma_2$  correspond to the  $\sigma$  variation of two different components. For a proper comparison between the theoretical bolometric values from our 3D models and the observational measurements, which are specific to the *Kepler* band pass, we have applied a bolometric correction following Ballot et al. (2011), as this was also the approach taken by K14. We have also tried the formalism by Lund (2019), who in addition to the approach by Ballot et al. (2011) (which assumes a black-body representation of the stellar spectrum) introduced the use of synthetic 1D atmosphere models (see Lund 2019, for further details).

In Fig. D1 we show the standard deviation of the stars from the LEGACY sample, corrected with the two different bolometric corrections. We can see that the differences among the corrected standard deviations due to the bolometric corrections are very small, which means that they do not affect the interpretation of our results when comparing the 3D models and observations.

$\xi_i$  in Eq. 10 must be determined on a star by star basis using the relation:

$$\xi_i = 2a_i \sin(\pi a_i^{-1}). \quad (11)$$

Finally,  $G(\nu)$  denotes the Gaussian envelope used to approximate the power excess from oscillations:

$$G(\nu) = P_g \exp \left( -\frac{(\nu - \nu_{\text{max}})^2}{2\sigma_g^2} \right), \quad (12)$$

where  $P_g$  gives the height of the Gaussian envelope,  $\nu_{\text{max}}$  gives the frequency of maximum power density, and  $\sigma_g$  gives the spread of the Gaussian envelope.

The background function was fitted in the interval from 3  $\mu$ Hz to the Nyquist frequency at  $\sim 8496 \mu$ Hz. We set such a lower limit on the frequency because the filtering of the data in the processing stage will inadvertently have an impact on the low-frequency part of the spectrum. The fit is performed in an MCMC manner using the *emcee* Python package (Foreman-Mackey et al. 2013)<sup>1</sup> – we refer to Lund et al. (2017) for details on the optimization. One of the three components in (10) is included to account for any low-frequency activity signal, while the other two (with the lowest timescales,  $\tau$ ) are treated as components related to the granulation.

Based on the background fit we compute from the MCMC chains the distribution from the combined  $\sigma$  signal of the two granulation-related components, by adding the respective  $\sigma_i$  values in quadrature. From the resulting distribution, we determine the median and uncertainties from the limits of the 68% highest probability density interval. The resulting total  $\sigma$  values are provided in Table 4.

Similar to the procedure adopted for the 3D simulations, we also compute a distribution for the effective e-folding timescale,  $\tau_{\text{ACF}}$ , of the combination of the two granulation components by sampling from the MCMC chains of the fit. The effective timescales are provided in Table 4.

<sup>1</sup> <https://github.com/dfm/emcee>

**Table 5.**  $\alpha$  values from the relations between  $\sigma$  with  $g$  and  $\nu_{\max}$  from Fig. 8.

Relation	$\alpha$ - 3D models	$\alpha$ - K14
$\log g \leq 3.5$		
$\sigma \propto g^\alpha$	$-0.609 \pm 0.037$	$-0.610 \pm 0.004$
$\sigma \propto \nu_{\max}^\alpha$	$-0.626 \pm 0.041$	$-0.624 \pm 0.005$
$\log g \geq 3.5$		
$\sigma \propto g^\alpha$	$-0.507 \pm 0.045$	$-0.529 \pm 0.025$
$\sigma \propto \nu_{\max}^\alpha$	$-0.510 \pm 0.044$	$-0.535 \pm 0.026$

## 4.2 Comparison with observational data

In this section, we compare both  $\sigma$  and  $\tau_{\text{ACF}}$  obtained from our 3D stellar atmosphere models with *Kepler* data, and we check if the 3D models can reproduce the observational data.

We first compare the  $\sigma$  values of our complete sample of 3D stellar atmosphere models –including all metallicities– with the values reported by K14. The comparison is made in terms of  $\nu_{\max}$  as shown in Fig. 8 and in terms of  $\log g$  in the Appendix C. Our 3D models agree very well with the results from K14, especially for stars with  $\log g \leq 3.5$ . This can be seen in the linear regressions (power laws) between our estimated  $\sigma$  and  $\nu_{\max}$  and  $\log g$ , which are summarized in Table 5. The relations derived using the 3D models agree within the uncertainties with the relations from K14, but we observe a slight deviation in  $\sigma \propto \nu_{\max}^\alpha$ , when  $\log g \geq 3.5$ . Our 3D models tend to have a higher  $\sigma$  than the ones found by K14 for stars with  $\log g \geq 4.0$  or  $\nu_{\max} \geq 1000 \mu\text{Hz}$ . We preferred to have two different fits above and below  $\log g = 3.5$  since it provides a better fit between our 3D models and observations, rather than a single one, indicating 2 possible trends in the data.

We would like to point out that including the 3D models at different metallicities results in a small scatter of  $\sigma$  at a given  $\log g$  or  $\nu_{\max}$ , which is also what we expected to obtain, as discussed in Sec. 3.3. Additionally, our models reproduce the scatter of the *Kepler* stars from K14.

We decided to have a close-up analysis on the stars with  $\log g \geq 3.5$ , by comparing our 3D models, K14 data, and LEGACY stars. Fig. 9 shows  $\sigma$  in terms of  $\nu_{\max}$  for the three data sets. We see that the LEGACY sample overlaps with some of the K14 stars, but also follows our 3D models with  $\log g \geq 4.4$  or  $\nu_{\max} \geq 3000 \mu\text{Hz}$ . Some of the 3D models have slightly higher values than the ones reported by observations, but this might also be due to the sparse sample of stars. Despite that, the theoretical and observational linear regressions are very similar within the 1-sigma error bars, as shown in Table 5.

Regarding the auto-correlation timescales, we calculated the ACF directly using the time series from the 3D models, whereas K14 used the two superposed granulation components from the fit to the power spectrum of each star. Fig. 9 shows the comparison of our timescales from the 3D models with the ones reported by K14 in terms of  $\nu_{\max}$ , and in terms of  $\log g$  in the Appendix C. As for the standard deviations, we derived two fits above and below  $\log g = 3.5$ , which are summarized in Table 6. On the one hand, the 3D models and observational timescales in general agree when  $\log g \leq 3.5$ . On the other hand, the timescales from our 3D sample do not fit K14 values when  $\log g \geq 3.5$ , and there is a clear offset between the 3D models and data from K14 of  $\sim 200 \mu\text{Hz}$  for the sub-giants, to  $\sim 500 \mu\text{Hz}$  for the MS stars. To further explore these discrepancies, we decided to compare with the timescales of the LEGACY sample as well, which

**Table 6.**  $\alpha$  values from the relations between  $\tau_{\text{ACF}}$  with  $\log g$  and  $\nu_{\max}$  from Fig. 9.

Relation	$\alpha$ - 3D models	$\alpha$ - K14
$\log g \leq 3.5$		
$\tau_{\text{ACF}} \propto g^\alpha$	$-1.028 \pm 0.023$	$-0.821 \pm 0.003$
$\tau_{\text{ACF}} \propto \nu_{\max}^\alpha$	$-1.060 \pm 0.027$	$-0.843 \pm 0.004$
$\log g \geq 3.5$		
$\tau_{\text{ACF}} \propto g^\alpha$	$-0.948 \pm 0.021$	$-0.901 \pm 0.013$
$\tau_{\text{ACF}} \propto \nu_{\max}^\alpha$	$-0.965 \pm 0.026$	$-0.951 \pm 0.014$

were computed by following a similar approach as K14 did, but with a more robust technique, as mentioned in Sec. 4.1.

The comparisons are illustrated in the right panel of Fig. 9 in terms of  $\nu_{\max}$ , which shows that the timescales from the LEGACY sample follow the trend depicted by the 3D models. Since the LEGACY sample included three stars also present in the sample from K14, we expected to reproduce their timescales, but that was not possible. One of the reasons behind the discrepancy between the timescales from K14 and the LEGACY sample is, that the former study fixed the exponents of the background models to 4, while they were set to be free parameters in the background models of the LEGACY sample, which is important since Mathur et al. (2011) showed that different background models provide slightly different results. Another reason might be the robustness of the method used in this work to determine the timescales, compared to the one used in K14, since we computed a distribution of  $\tau_{\text{ACF}}$  using MCMC. Additionally, the horizontal offset in Fig. 9 between the LEGACY sample and data from K14 might also be due to having more accurate stellar parameters derived with asteroseismology, as is the case for the LEGACY sample. Therefore, this analysis suggests that the stars analyzed in K14 using scaling relations introduced some biases in the granulation power laws.

## 5 DISCUSSION

Several studies have determined granulation properties in terms of standard deviations and auto-correlation times ( $\sigma$ , and  $\tau_{\text{ACF}}$ ) for stars observed by the *Kepler* mission (i.e. Mathur et al. (2011); K14; Kallinger et al. (2016); Corsaro et al. (2017)). Additionally, several attempts have been made to compare these values with 3D stellar atmosphere models (i.e. Mathur et al. (2011); Tremblay et al. (2013); Samadi et al. (2013); Ludwig & Steffen (2016)).

Mathur et al. (2011) analyzed the power spectra of approximately 1000 red giants with six different methods, all based on Harvey profiles, similar to for our treatment of the LEGACY sample. They found an overall agreement among the six methods since they all showed that the granulation power and  $\tau_{\text{ACF}}$  increase with decreasing  $\nu_{\max}$ , as we also reproduced in this study. However, the six methods did not retrieve the same values of granulation power or  $\tau_{\text{ACF}}$ , due to the systematic differences associated with the choice of background fitting method. Tremblay et al. (2013) arrived to a similar conclusion by modeling the power spectrum of 3D stellar atmosphere models with different expressions, which resulted in significantly different timescales. Still, Mathur et al. (2011) reported general relations for the granulation properties, where  $\sigma \propto \nu_{\max}^{-0.45}$ , similar to the values we found for the 3D models with  $\log g \geq 3.5$ . They found an auto-correlation time  $\tau_{\text{ACF}} \propto \nu_{\max}^{-0.89}$ , which is an average between the timescales derived from all six methods. It shows a lower coefficient

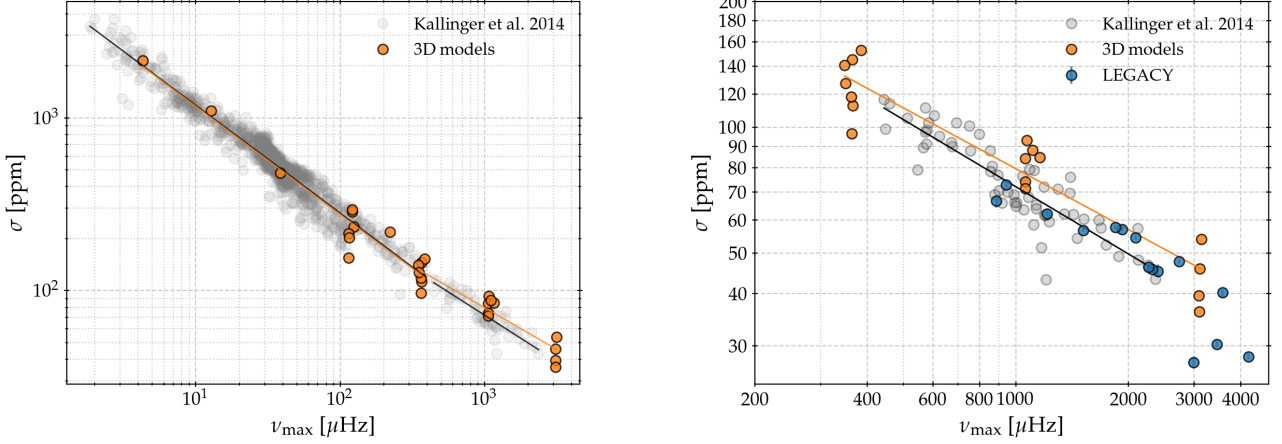


**Figure 8.** Standard deviation  $\sigma$  comparison between our 3D sample and *Kepler* data from K14 as function of  $\nu_{\max}$ . The orange lines are linear regressions of our data, while the black ones correspond to K14. For both cases, we make two kinds of fits: one for stars and models with  $\log g \leq 3.5$ , and the other for  $\log g \geq 3.5$ . In the right panel, we present a zoom-in comparison for  $\log g \geq 3.5$ , where we added the Legacy sample.

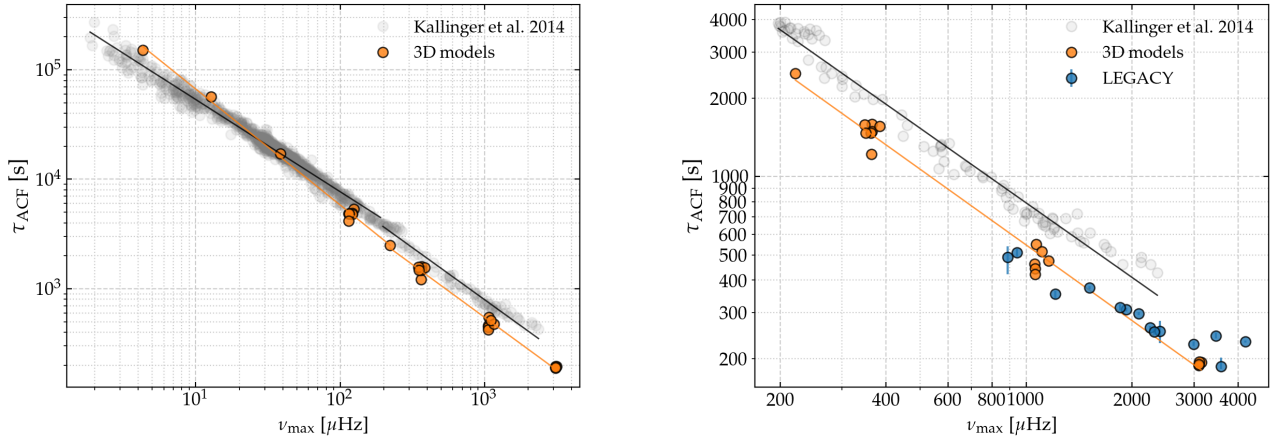


**Figure 9.** Auto-correlation time  $\tau_{\text{ACF}}$  comparisons between our 3D sample and *Kepler* data from K14, as functions of  $\nu_{\max}$ . The orange lines are linear regressions of our data, while the black ones correspond to K14. For both cases, we make two kinds of fits: one for stars and models with  $\log g \leq 3.5$ , and the other for  $\log g \geq 3.5$ . In the right panel, we present a zoom-in comparison for  $\log g \geq 3.5$ , adding the Legacy sample. Our 3D models agree with the Legacy sample, while there is an offset with K14 indicating a possible problem in stellar parameter determination.

than the ones we reported in Table 6 for our 3D models, but their relation is similar to the  $\alpha$  values found for the sample of K14.

Mathur et al. (2011) compared as well their values with 3D models of red giants at solar metallicities, which belong to the grid described in Trampedach et al. (2013). They reported that both the effective timescales and granulation power of the simulations decrease as  $\nu_{\max}$  increases, as shown in this study. However, their timescales were overestimated and granulation power laws were underestimated when compared with observational data, which is not the case in our study, since we reproduce both the observed  $\sigma$  and timescales. They argued that the discrepancies might be due to only having models at solar metallicity, or stellar radii with insufficient accuracy, among other explanations. Based on our results, we do acknowledge that metallicity has an impact on  $\sigma$ , hence the granulation power, and  $\tau_{\text{ACF}}$ , but it cannot cause a systematic shift of these quantities as shown in Fig. 11 in Mathur et al. (2011). Moreover, as shown in Fig. 6, for a given set of  $T_{\text{eff}}$ - $\log g$ , the quantities  $\sigma$  and  $\tau_{\text{ACF}}$  decrease slowly

with metallicity and cannot compensate the discrepancies reported by them. Similarly, we point out that, even though inaccurate stellar radii associated with the 3D models do affect the standard deviation, the results should be more scattered rather than systematically shifted. Thus, we attribute the discrepancies to the short time series of the 3D models used in Mathur et al. (2011), and possibly to the presence of box modes (see Appendix A).

We also compared our results with Samadi et al. (2013) as shown in Fig. 7. They analyzed their 3D models by modeling the power density spectrum and derived the  $\sigma$  brightness fluctuations from it. However, their  $\sigma$  values have strong scatter if expressed only in terms of  $\nu_{\max}$ , while the scatter of  $\tau_{\text{ACF}}$  is less significant. The scatter is so critical, that for models with  $\nu_{\max}$  above  $1000 \mu\text{Hz}$ , they predicted that  $\sigma$  can oscillate 80 ppm for a given  $\nu_{\max}$  and, in some cases, fluctuate between two orders of magnitude.

To find a better correlation with stellar parameters, they proposed new scaling relations for both quantities with a dependency on the

Mach number, i.e. the ratio between the convective velocity and the sound speed. Thus, it is a difficult quantity to obtain for observed stars. On the contrary, our 3D models and their standard deviation of the brightness fluctuations clearly follow a simple power law in terms of  $\nu_{\max}$ . Hence, we show that it is not necessary to include the Mach number dependence in the scaling relations. Even though we do not explore the relationship with the Mach number, we refer the reader to Tremblay et al. (2013) for a discussion about the granulation properties in terms of the Mach number.

K14 expanded the study made by Mathur et al. (2011) by including MS stars, and tested several methods to model the granulation background signal using a probabilistic approach. They originally reported that  $\sigma \propto \nu_{\max}^{-0.61}$ , but derived as well a relation dependant on the stellar mass to follow the 3D models from Samadi et al. (2013). However, we do want to point out that we observed the same behavior in the LEGACY stars analyzed in this sample, so the change of trend is unlikely to be associated with the method used to analyze both 3D models and stars. Future studies that decide to explore this problem should focus on adding more MS stars at different metallicities with accurate stellar parameters. Additionally, more 3D models with, for instance,  $\nu_{\max} = 600 \mu\text{Hz}$  or  $2000 \mu\text{Hz}$  should be added to fill in the gaps shown in Fig. 8. Regarding the timescales,  $\tau_{\text{ACF}}$  has a different behavior than the relation derived with observational data from K14 for  $\log g \leq 3.5$ . For the case  $\log g \geq 3.5$  we see that the theoretical and observational relations are more similar, but still not the same. Additionally, there seems to be an offset between the 3D models and LEGACY sample with K14. These discrepancies might arise due to the accuracy of the stellar parameters, or the different methods used to model the power spectrum density, as Mathur et al. (2011) found out. Thus, it seems that the function to fit the power spectrum density has a great impact on the derived timescale, as Tremblay et al. (2013) suggested as well. Since the LEGACY sample reproduces the timescales from our 3D models, we propose that the fits to the power spectrum of stars keep the exponent as a free parameter, contrary to what K14 did.

We attempted to derive the timescales as Kallinger et al. (2016) proposed, that is, by fitting a  $\text{sinc}^2$  function to the ACF of filtered time series of *Kepler* stars, which had the combined contribution of granulation and p-mode oscillations. We note that they did not actually include the factor of four in the fit proposed in the Supplementary Materials (Kallinger et al. 2016) in their calculations, so we did not use it either. However, we could not reproduce the observed timescales, since our values were almost overestimated by a factor of two. One of the reasons might be due to the p-mode contribution from the observational data since our 3D models did not have any contribution from oscillations.

Lastly, we comment on the effect of metallicity on  $\sigma$ . To our knowledge, Ludwig & Steffen (2016) is the only previous theoretical study focused on that problem, using 3D stellar atmosphere models from the CIFIST grid with metallicities equal to  $[\text{Fe}/\text{H}] = 0.0$  and  $-2.0$ . Even though their  $\sigma$  also increases with decreasing  $\nu_{\max}$ , their data are scattered for both metallicities, similarly as the data presented in Samadi et al. (2013). This is not surprising, since they also used CIFIST 3D models, but employed a different method to determine  $\sigma$ . Therefore, the dispersion on the data might not be attributed to the method, but possibly to other factors, such as the length of the time series, or the radius determination of a given simulation, since it is a difficult quantity to compute by only providing atmospheric parameters. Moreover, Ludwig & Steffen (2016) also claimed that they could not provide a fit for  $\sigma$  in terms of  $[\text{Fe}/\text{H}]$  using their models at  $[\text{Fe}/\text{H}] = 0.0$  and  $[\text{Fe}/\text{H}] = -2.0$  simultaneously, and neither could reproduce the  $\sigma$  values from K14, at least using the 3D models at

solar metallicity. However, in Fig. 8 we showed that we can provide a fit to all our 3D models together and we can reproduce the results from K14 (see Sec. 4.2).

## 6 CONCLUSIONS

Thanks to photometric data from space missions, the study and characterization of the stochastic brightness fluctuations of stars has been possible. In this study we aimed to study in detail the granulation properties of these stochastic brightness fluctuations, by using 3D stellar atmosphere models distributed across the HR diagram, at different metallicities. Particularly, the granulation properties that we determined were the standard deviation of the granulation noise  $\sigma$  and the characteristic timescale  $\tau_{\text{ACF}}$ . For these 3D models, we computed very long time series that covered at least 1000 turnover convective times, in order to have a standard deviation independent of the length of the time series. Unlike previous studies, and for the first time, we show that both standard deviation and auto-correlation time follow some power laws in terms of only  $\nu_{\max}$  or  $\log g$ . This means that we only need to determine accurate stellar parameters to derive two properties associated to granulation. For the solar metallicity case, we found that  $\sigma \propto \nu_{\max}^{-0.567}$  and  $\tau_{\text{ACF}} \propto \nu_{\max}^{-0.997}$ . This shows that, we did not need to introduce the Mach number in our power laws to describe the dependence of granulation properties on stellar parameters, which is a difficult quantity to determine from stellar observational constraints, since some assumptions have to be made in order to express the Mach number in terms of the fundamental parameters ( $T_{\text{eff}}$ ,  $\log g$ ,  $[\text{Fe}/\text{H}]$ ). However, the present work shows that the introduction of this quantity is not needed to reproduce the observed granulation properties. Moreover, we found that both  $\sigma$  and  $\tau_{\text{ACF}}$  decrease with metallicity with a power law dependence in terms of  $\nu_{\max}$ , that we derived for  $[\text{Fe}/\text{H}] = 0.0, -0.5, -1.0, -2.0$ , which means that metallicity does need to be taken into account when deriving granulation properties.

To validate our theoretical results and power laws, we compared with a large sample of *Kepler* stars from K14, and selected stars from the LEGACY sample (Lund et al. 2017), since they have accurate stellar parameters. Unlike previous studies, we found that our 3D stellar atmosphere models agree very well with the granulation noise from *Kepler* stars, especially at  $\log g \leq 3.5$ . We think that the comparison between stars and 3D models for  $\log g \geq 3.5$  can be improved if more targets are added in that regime. Regarding the relationship between  $\tau_{\text{ACF}}$  and  $\nu_{\max}$ , we found that 3D models reproduced the timescales of the selected stars of the LEGACY sample, but did not fully reproduced the timescales from the K14 sample. We think that this is because the stars from the LEGACY sample have accurate stellar parameters i.e., accurate  $\nu_{\max}$ , while the  $\nu_{\max}$  values of the stars from the K14 sample were derived with asteroseismic scaling relations.

With this study we intended to provide better scaling relations to characterize the convective granulation noise, so that we can better understand the signature of granulation in the time series of stellar targets, and hence, improve the detection and characterization of exoplanets. In a future work, we plan to expand this study by performing a full monochromatic radiative transfer within the *Kepler*, or *PLATO* bandwidths, including the response functions of these instruments.



## ACKNOWLEDGEMENTS

Funding for the Stellar Astrophysics Centre is provided by The Danish National Research Foundation (Grant agreement no.: DNR106). L. F. R. D. and V. A. B.-K. acknowledges support from the Independent Research Fund Denmark (Research grant 7027-00096B) and the Carlsberg foundation (grant agreement CF19-0649). The numerical results presented in this work were obtained at the Centre for Scientific Computing, Aarhus <http://phys.au.dk/forskning/cscaa/>. Part of the calculations have also been performed using the OCA/SIGAMM mesocentre. This research was undertaken with the assistance of resources provided at the NCI National Facility systems at the Australian National University through the National Computational Merit Allocation Scheme supported by the Australian Government. This work was supported by the “Programme National de Physique Stellaire” (PNPS) of CNRS/INSU co-funded by CEA and CNES.”

## DATA AVAILABILITY

Data available on request. The data underlying this article will be shared on reasonable request to the corresponding author.

## REFERENCES

- Aguirre Børsen-Koch V., et al., 2021, *MNRAS*,  
 Baglin A., et al., 2006, in 36th COSPAR Scientific Assembly. p. 3749  
 Ballot J., Barban C., van’t Veer-Menneret C., 2011, *A&A*, **531**, A124  
 Barros S. C. C., Demangeon O., Díaz R. F., Cabrera J., Santos N. C., Faria J. P., Pereira F., 2020, *A&A*, **634**, A75  
 Bastien F. A., Stassun K. G., Basri G., Pepper J., 2013, *Nature*, **500**, 427  
 Bastien F. A., Stassun K. G., Basri G., Pepper J., 2016, *The Astrophysical Journal*, **818**, 43  
 Belkacem K., Goupil M. J., Dupret M. A., Samadi R., Baudin F., Noels A., Mosser B., 2011, *A&A*, **530**, A142  
 Borucki W. J., et al., 2010, *Science*, **327**, 977  
 Bugnet L., García R. A., Davies G. R., Mathur S., Corsaro E., Hall O. J., Rendle B. M., 2018, *A&A*, **620**, A38  
 Chaplin W. J., et al., 2011a, *Science*, **332**, 213  
 Chaplin W. J., et al., 2011b, *ApJ*, **732**, 54  
 Collet R., Asplund M., Trampedach R., 2007, *A&A*, **469**, 687  
 Collet R., Nordlund A., Asplund M., Hayek W., Trampedach R., 2018, *MNRAS*, **475**, 3369  
 Corsaro E., et al., 2017, *A&A*, **605**, A3  
 Cranmer S. R., Bastien F. A., Stassun K. G., Saar S. H., 2014, *ApJ*, **781**, 124  
 Foreman-Mackey D., Hogg D. W., Lang D., Goodman J., 2013, *PASP*, **125**, 306  
 Gustafsson B., Edvardsson B., Eriksson K., Jørgensen U. G., Nordlund A., Plez B., 2008, *A&A*, **486**, 951  
 Handberg R., Lund M. N., 2014, *MNRAS*, **445**, 2698  
 Harvey J., 1985, in Rolfe E., Battrick B., eds, *ESA Special Publication Vol. 235, Future Missions in Solar, Heliospheric & Space Plasma Physics*. p. 199  
 Hayek W., Asplund M., Carlsson M., Trampedach R., Collet R., Gudiksen B. V., Hansteen V. H., Leenaarts J., 2010, *A&A*, **517**, A49  
 Hidalgo S. L., et al., 2018, *ApJ*, **856**, 125  
 Howell S. B., et al., 2014, *PASP*, **126**, 398  
 Kallinger T., et al., 2014, *A&A*, **570**, A41  
 Kallinger T., Hekker S., García R. A., Huber D., Matthews J. M., 2016, *Science Advances*, **2**, 1500654  
 Kjeldsen H., Bedding T. R., 2011, *A&A*, **529**, L8  
 Ludwig H.-G., 1992, PhD thesis, University of Kiel, Germany  
 Ludwig H. G., 2006, *A&A*, **445**, 661  
 Ludwig H. G., Steffen M., 2013, *Memorie della Societa Astronomica Italiana Supplementi*, **24**, 53  
 Ludwig H. G., Steffen M., 2016, *Astronomische Nachrichten*, **337**, 844  
 Ludwig H. G., Caffau E., Steffen M., Freytag B., Bonifacio P., Kučinskas A., 2009, *Memorie della Società Astronomica Italiana*, **80**, 711  
 Lund M. N., 2019, *MNRAS*, **489**, 1072  
 Lund M. N., et al., 2017, *ApJ*, **835**, 172  
 Magic Z., Collet R., Asplund M., Trampedach R., Hayek W., Chiavassa A., Stein R. F., Nordlund A., 2013, *A&A*, **560**, A8  
 Mathur S., et al., 2011, *ApJ*, **741**, 119  
 Meunier N., Lagrange A. M., 2020, *A&A*, **642**, A157  
 Michel E., Samadi R., Baudin F., Barban C., Appourchaux T., Auvergne M., 2009, *A&A*, **495**, 979  
 Mihalas D., Dappen W., Hummer D. G., 1988, *ApJ*, **331**, 815  
 Ness M. K., Silva Aguirre V., Lund M. N., Cantiello M., Foreman-Mackey D., Hogg D. W., Angus R., 2018, *ApJ*, **866**, 15  
 Nordlund A., 1982, *A&A*, **107**, 1  
 Nordlund A., Dravins D., 1990, *A&A*, **228**, 155  
 Nordlund A., Galsgaard K., 1995, Technical report, A 3D MHD code for Parallel Computers  
 Nordlund Å., Stein R. F., 2001, *The Astrophysical Journal*, **546**, 576  
 Nordlund Å., Stein R. F., Asplund M., 2009, *Living Reviews in Solar Physics*, **6**, 2  
 Pande D., Bedding T. R., Huber D., Kjeldsen H., 2018, *MNRAS*, **480**, 467  
 Pereira F., et al., 2019, *MNRAS*, **489**, 5764  
 Rauer H., et al., 2014, *Experimental Astronomy*, **38**, 249  
 Ricker G. R., et al., 2015, *Journal of Astronomical Telescopes, Instruments, and Systems*, **1**, 014003  
 Salaris M., Chieffi A., Straniero O., 1993, *ApJ*, **414**, 580  
 Samadi R., et al., 2013, *A&A*, **559**, A40  
 Silva Aguirre V., et al., 2015, *MNRAS*, **452**, 2127  
 Silva Aguirre V., et al., 2017, *ApJ*, **835**, 173  
 Skartlien R., 2000, *ApJ*, **536**, 465  
 Stein R. F., Nordlund Å., 2003, in Hubeny I., Mihalas D., Werner K., eds, *Astronomical Society of the Pacific Conference Series Vol. 288, Stellar Atmosphere Modeling*. p. 519 ([arXiv:astro-ph/0209510](https://arxiv.org/abs/astro-ph/0209510))  
 Sulis S., Mary D., Bigot L., 2020a, *A&A*, **635**, A146  
 Sulis S., Lendl M., Hofmeister S., Veronig A., Fossati L., Cubillos P., Van Grootel V., 2020b, *A&A*, **636**, A70  
 Trampedach R., Christensen-Dalsgaard J., Nordlund A., Stein R. F., 1998, in Kjeldsen H., Bedding T. R., eds, *The First MONS Workshop: Science with a Small Space Telescope*. p. 59  
 Trampedach R., Asplund M., Collet R., Nordlund Å., Stein R. F., 2013, *ApJ*, **769**, 18  
 Tremblay P. E., Ludwig H. G., Freytag B., Steffen M., Caffau E., 2013, *A&A*, **557**, A7  
 Van Kooten S. J., Anders E. H., Cranmer S. R., 2021, *ApJ*, **913**, 69  
 Viani L. S., Basu S., Chaplin W. J., Davies G. R., Elsworth Y., 2017, *ApJ*, **843**, 11  
 Yu J., Huber D., Bedding T. R., Stello D., Hon M., Murphy S. J., Khanna S., 2018, *ApJS*, **236**, 42

## APPENDIX A: EFFECTS OF THE SIMULATION SETUP

The brightness fluctuations are intimately linked to radiative losses at the surface. Therefore the numerical treatment of radiative transport in the RHD code might affect our results. In this section we summarize the impact that different setups have on the brightness fluctuations from the 3D stellar atmosphere models. Specifically, we analyzed the number of bins included in the opacity tables, the number of rays used to solve the Radiative Transfer (RT) equation, the spatial grid resolution and, the presence of box-modes.

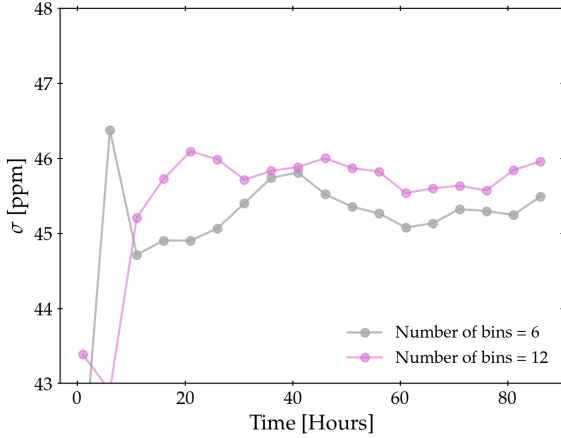


**Figure A1.** Effect of a 6-bin and a 12-bin opacity tables on the  $\sigma$  calculated from the relative flux variations of two 3D solar models, computed with the same setup.

### A1 Number of opacity bins

The number of bins used in the generation of an opacity table determines the accuracy of the radiative heating and cooling rates of each 3D stellar model. This means, that both the temperature stratification and the temperature fluctuations of every model are affected by the choice of number of bins, and how they are selected. Therefore, to test the effect of the number of bins on the brightness fluctuations, two opacity tables, with 6 and 12 bins respectively, were used to create two solar models with the same setup. The time series generated for every model cover approximately 80 hours.

Fig. A1 shows the  $\sigma$  of brightness fluctuations calculated from the relative flux variations. The  $\sigma$  was calculated with cumulative intervals of 5 hours as well.

The initial  $\sigma$  values fluctuate significantly in both solar simulations as a result of the convection itself, and not as a consequence of the bin schemes in each opacity table. The  $\sigma$  of both simulations evolve in a similar fashion and take very similar values. Consequently, we can conclude that the number of bins will not affect the  $\sigma$  associated with the relative flux variations, as Tremblay et al. (2013) also suggested. Therefore, we decided to compute our 3D stellar models using a 6-bin opacity table, since it is less computationally expensive.

### A2 Number of rays used in radiative transfer

In the STAGGER-code, the radiative transfer equation can be solved along a vertical ray or a combination of vertical plus inclined rays. When only a vertical ray is used, the stratifications of the thermodynamic variables are usually overestimated, including the effective temperature of the stars. This occurs because the stellar model assumes that all the radiation coming from the bottom boundary of the simulation travels vertically, which is not a realistic approach. On the other hand, the combination of one vertical ray plus one inclined, or one vertical and two inclined produce more accurate representations of the stellar atmospheres.

In order to test the response of the brightness fluctuations based on the number of rays, three solar simulations were generated with the three combinations of rays previously mentioned. The results obtained are shown in Fig. A2, where an overestimation of the  $\sigma$  is obtained when only one vertical ray is used. This is a consequence of

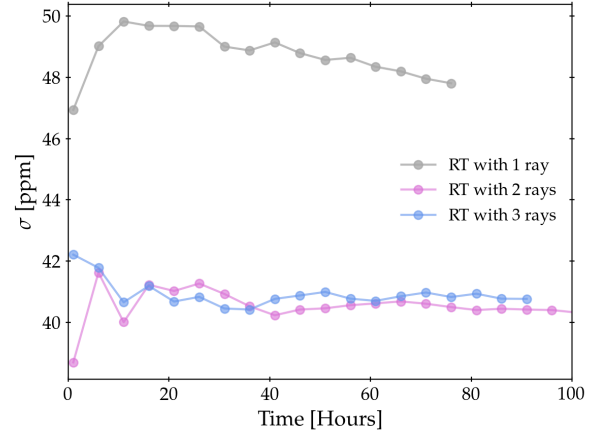


**Figure A2.** Effect of the number of rays used to solve the Radiative Transfer equation on the  $\sigma$  of brightness fluctuations. This was calculated from the relative flux variations of three 3D solar models with identical setup. The gray series shows the one-vertical ray case, the pink series illustrates the case with two rays: one vertical plus one inclined. Finally, the blue series represents the case with three rays: one vertical plus two inclined.

the overestimation of the radiative flux, as it was mentioned before. On the contrary, the cases including at least one inclined ray show that  $\sigma$  converges to the same value after 20 hours. In other words, using two or three rays to solve the radiative transfer equation results in basically the same  $\sigma$ . Since creating a 3D stellar model is less computationally expensive if only two rays – one inclined and one vertical – are used, we decided to compute our sample of 3D models with that configuration.

### A3 Effect of grid resolution and box-modes

The 3D stellar models computed with the STAGGER-code have typically the following grid resolutions: low resolution, where every direction has 120 points; and high resolution, where each has 240 points. Furthermore, the simulations also include box-modes Nordlund & Stein (2001), which are acoustic modes generated by both the stochastic excitation and the work done by the bottom boundary. These modes have, however, excessively large amplitudes, due to the shallow nature of the simulation boxes and, consequently, due to their very low inertia.

In order to assess the possible impacts of both the resolution and box modes, four solar models were created as follows:

- (i) Damping of box modes and low resolution ( $120^3$ ).
- (ii) Damping of box modes and high resolution ( $240^3$ ).
- (iii) No damping of box modes and low resolution ( $120^3$ ).
- (iv) No damping of box modes and high resolution ( $240^3$ ).

The  $\sigma$  from these 3D models are shown in Fig. A3. It can be seen that the resolution does not have a significant influence on the results, if the time series are long enough, which is the case for our models. Thus, we decided to compute the models listed in Table 1 in the low resolution regime, for computational purposes.

On the other hand, the box modes do have a significant impact on  $\sigma$ , especially in the low resolution models. However, since the large box mode amplitudes of the simulations overestimate the observed modes in stars, we think that damping the box modes provides a more reliable approach for this study.

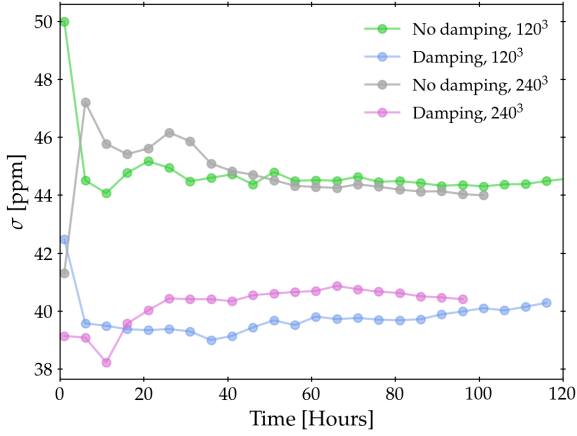


**Figure A3.** Effect of the resolution and box modes on the  $\sigma$  calculated from the relative flux variations of 3D solar models, computed with the same setup.

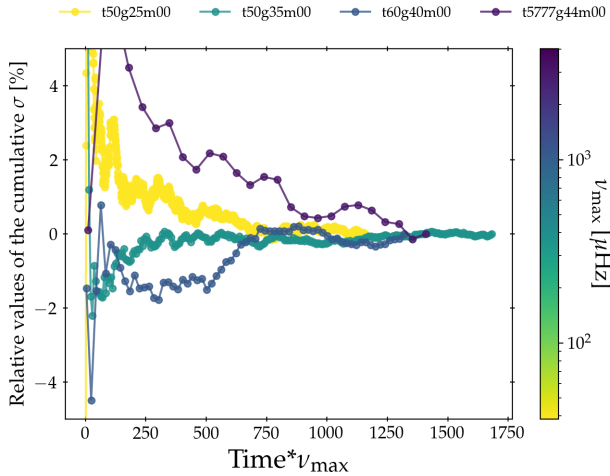


**Figure B1.** Relative  $\sigma$  for four different 3D stellar atmosphere models at solar metallicity, as a function of the number of convective turnover times.

## APPENDIX B: $\sigma$ OF THE RELATIVE BRIGHTNESS FLUCTUATIONS

Fig. B1 shows the convergence of  $\sigma$  on four different 3D stellar atmosphere models, and the importance of having very long time series.

## APPENDIX C: COMPARISON OF STANDARD DEVIATION IN TERMS OF SURFACE GRAVITY

In this section we show the standard deviation  $\sigma$  and the auto-correlation timescales  $\tau_{ACF}$  in terms of surface gravity  $\log g$ . Fig. C1 shows the comparison of the standard deviation with surface gravity, while Fig. C2 shows the auto-correlation timescales in terms of surface gravity.

## APPENDIX D: EFFECT OF BOLOMETRIC CORRECTION ON THE STANDARD DEVIATION OF THE LEGACY SAMPLE

As mentioned in Sec. 4.1, we decided to test the effect of the bolometric correction just on the LEGACY sample. We compared the formalism proposed by Ballot et al. (2011), where  $C_{bol} = (T_{eff}/T_0)^\alpha$  with  $T_0 = 5934$  K and  $\alpha = 0.8$ , with the formalism by Lund (2019), who used two methods to calculate the bolometric correction. The first method is assuming a stellar black-body (Planck) spectrum, similar to Ballot et al. (2011), while the second method uses 1D atmosphere models (see Lund 2019, for further details).

In Fig. D1 we show the standard deviation of the stars from the LEGACY sample, corrected with the three different bolometric corrections. We can see that the differences among the corrected standard deviations due to the bolometric corrections are very small –less than 5 ppm in all targets–, which means that they do not affect the interpretation of our results when comparing the 3D models and observations.

## APPENDIX E: POWER SPECTRA FITTING FOR THE SELECTED STARS OF THE LEGACY SAMPLE

Here we show the components of the background model to the power spectra of the selected sample of LEGACY stars, as was explained in Section 4.1. Fig. E1 shows the different components of the background model for the star KIC 6679371.

This paper has been typeset from a  $\text{\LaTeX}$  file prepared by the author.

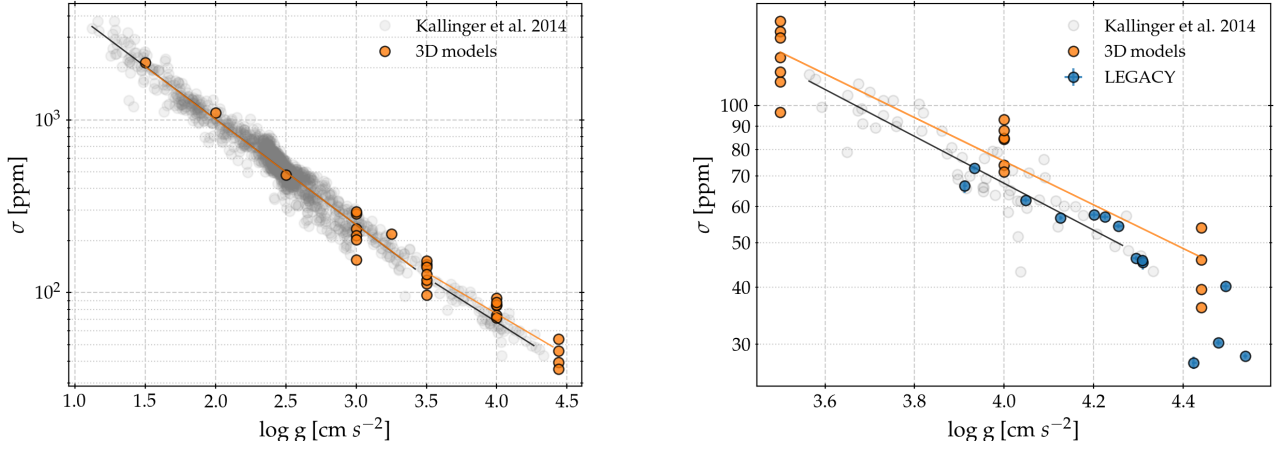


**Figure C1.** Similar to Fig. 8, where we show the comparison between the standard deviation  $\sigma$  of our 3D sample and *Kepler* data from K14 as function of  $\log g$ . The orange lines are linear regressions of our data, while the black ones correspond to K14. For both cases, we make two kinds of fits: one for stars and models with  $\log g \leq 3.5$ , and the other for  $\log g \geq 3.5$ . In the right panel, we present a zoom-in comparison for  $\log g \geq 3.5$ , adding the Legacy sample. In Table 5 we summarize the values for the relation in between  $\sigma$  and  $g$ .

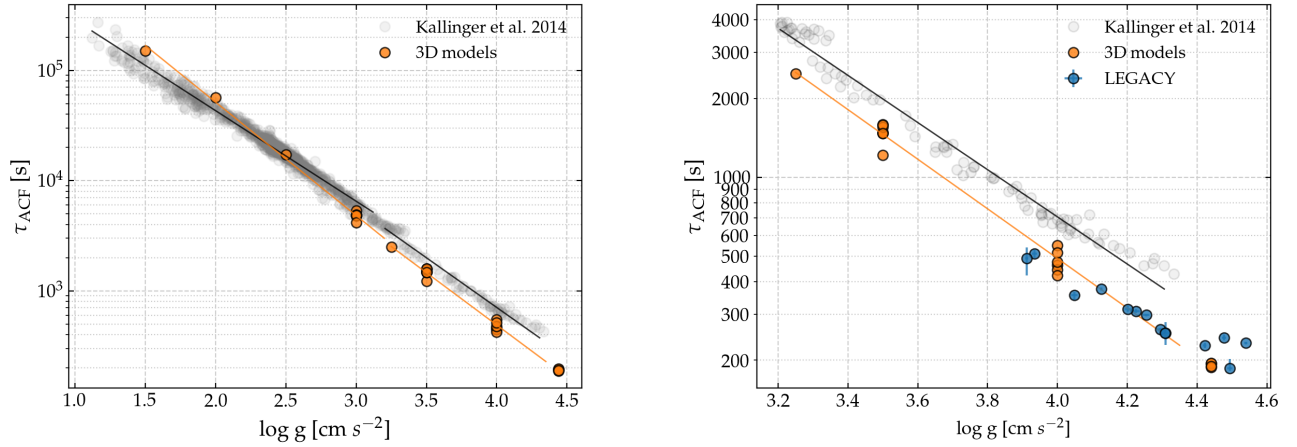


**Figure C2.** Similar to Fig. 9, where we show the comparison between the auto-correlation time  $\tau_{ACF}$  of our 3D sample and *Kepler* data from K14 as function of  $\log g$ . The orange lines are linear regressions of our data, while the black ones correspond to K14. For both cases, we make two kinds of fits: one for stars and models with  $\log g \leq 3.5$ , and the other for  $\log g \geq 3.5$ . In the right panel, we present a zoom-in comparison for  $\log g \geq 3.5$ , adding the Legacy sample. In Table 6 we summarize the values for the relation in between  $\sigma$  and  $g$ .



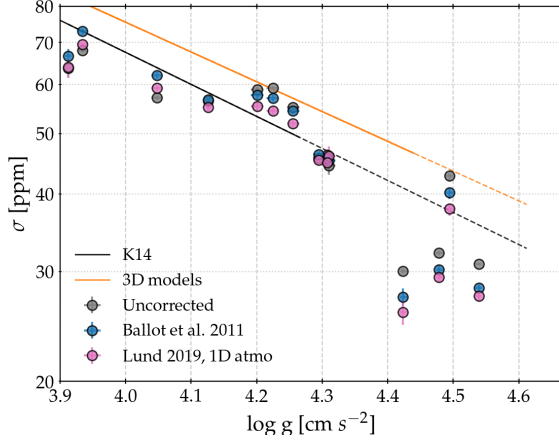


**Figure D1.** Comparison of the standard deviation values for the LEGACY sample, corrected using the two different approaches to calculating the bolometric correction. In grey, we show the uncorrected values; in blue the ones corrected the formalism by Ballot et al. (2011), corresponding to the values used in our work; and in pink the ones corrected using the synthetic 1D atmosphere approach by Lund (2019). For comparison, we have included the linear regression relations from our 3D sample (orange line) and the corresponding from K14 (black line). We extrapolated both relations for visualization, which are shown as dashed lines.

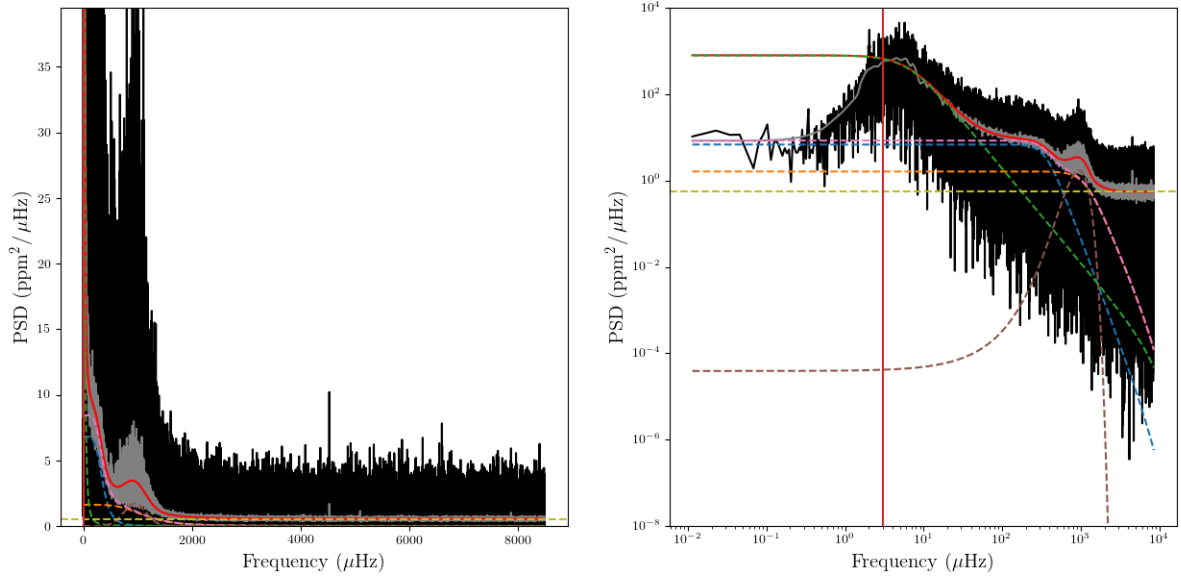


**Figure E1.** Example of background model to the power spectra of KIC 6679371. A similar approach was applied to all the selected targets of the LEGACY sample. The blue and orange dashed fits correspond to the first and second granulation component, while the pink dashed line is the sum of the the two granulation components. The green dashed fit represents the activity contribution, the yellow dashed line is the white noise level, and the brown fit corresponds to the p-mode contribution. The total model is the solid red fit.